# DEVELOPMENT FOR A FLEXIBLE GEAR WHEEL DYNAMICS SIMULATION ALGORITHM

*Master's degree in automotive engineering, academic year 2025/2026*

*Daniel D'Agostino S331622*


*Teaching staff:*

*Prof. Sorniotti Aldo*

*Dott. Bruzzone Fabio*

*Prof. Rosso Carlo*

# INDEX



# TABLES & FIGURES

***A Mamma e Papà***
***Grazie di tutto***

# ABSTRACT

In this study, the dynamic response of a spur gear pair is analyzed using a novel nonlinear approach. The actual rolling motion and gear engagement are simulated through a set of reduced-order models obtained in a pre-processing phase, using the minimum number of master's degrees of freedom without loss of accuracy or generality. Gear body flexibility is included by means of a refined finite element model, while all sources of nonlinearity are retained and no geometric simplifications are introduced.

To reduce computational cost, the time-varying meshing stiffness is precomputed and applied according to the instantaneous loading conditions. Contact loss and recovery are considered, with reconnection events modeled as vibro-impacts. The proposed method achieves a computational cost several orders of magnitude lower than models with comparable accuracy.

The results are validated against high-quality experimental data under different loading conditions during sweep-up and sweep-down maneuvers. In particular, the dynamic transmission error is analyzed, showing remarkable agreement with the experimental campaign. Complex nonlinear phenomena, such as hysteretic jumps, multiple resonances, and sub- and super-harmonic responses, are accurately predicted in terms of both frequency and amplitude.

The proposed approach enables fast and accurate nonlinear dynamic analyses of gear systems, overcoming current modeling limitations, and is suitable for future extensions to include additional components and effects.

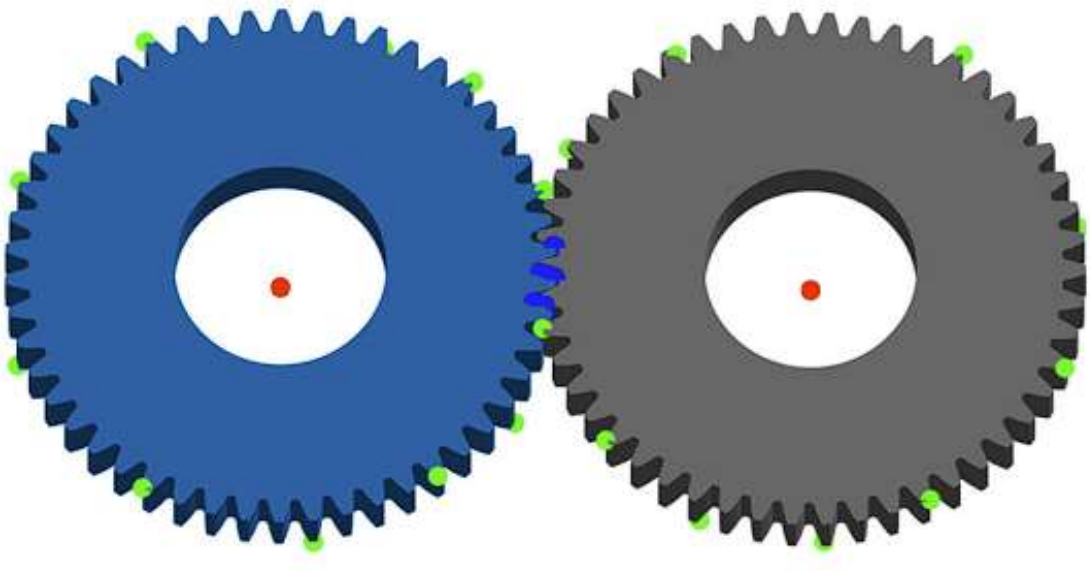

*Figure 1: Gear pair coupled with nodes highlighted*

# METHODOLOGY

The proposed approach is based on a modal reduction of axially symmetric finite element models using the Craig–Bampton Component Mode Synthesis (CMS) technique. This reduction allows the selection of a minimal set of master's degrees of freedom while preserving the accuracy of the original high-fidelity models.

The gear rotation is discretized into angular steps, and the system matrices are updated at each angular position to accurately represent the actual rolling motion and gear engagement throughout the meshing cycle.

$$\mathbf{u} = \begin{bmatrix} \mathbf{u}_m \\ \mathbf{u}_s \end{bmatrix} = \begin{bmatrix} \mathbf{I} & \mathbf{0} \\ \mathbf{\Phi}_c & \mathbf{\Phi}_n \end{bmatrix} \begin{bmatrix} \mathbf{q}_m \\ \mathbf{q}_n \end{bmatrix} \quad (1)$$

*Equation 1: physical displacement vector*

Within the reduced-order model, different types of nodes are defined according to their role in dynamic analysis. Contact stiffness nodes are introduced at the gear meshing interfaces and represent the primary source of nonlinearity in the system. Additional auxiliary observed nodes are included to enhance the accuracy of the reduced model, particularly in capturing local deformation effects. Virtual central nodes are also defined to apply the input torque and to extract the dynamic transmission error (DTE) as an output quantity.

$$\mathbf{M}_r = \mathbf{T}^T\mathbf{M}\mathbf{T} \qquad \mathbf{K}_r = \mathbf{T}^T\mathbf{K}\mathbf{T} \quad (2)$$

*Equation 2: reduced mass and stiffness matrices*

The time-varying mesh stiffness (TVMS) is precomputed for different load levels to significantly reduce the computational effort during the dynamic simulations. During the time integration, the stiffness is updated as a function of both the instantaneous angular position and the applied load.

$$\boldsymbol{K_r(\theta_i, T) = K_{struct} + K_{mesh}(\theta_i, T)} \quad (3)$$

*Equation 3: angular discretization of gear rotation*

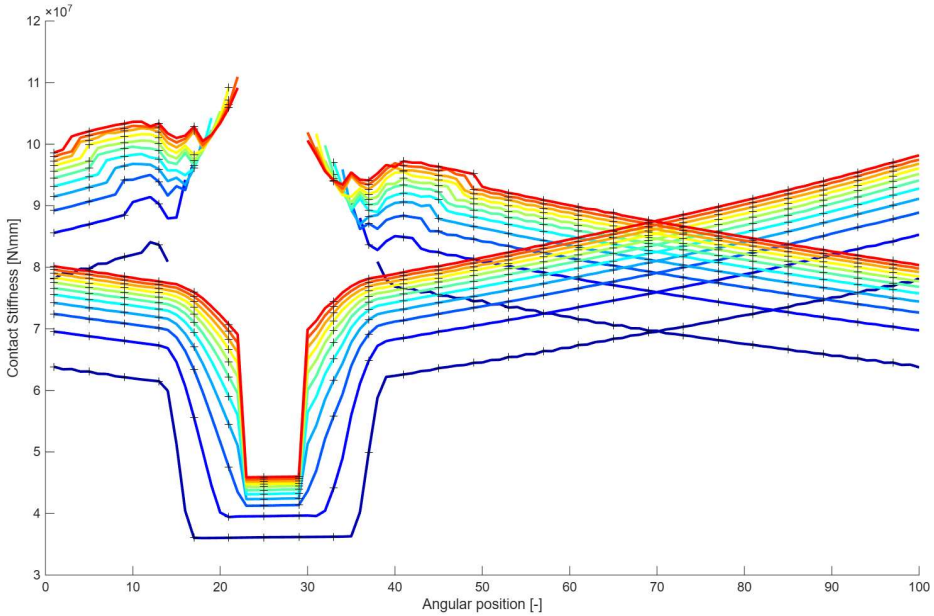


*Figure 2: TVMS map for torques from 10 to 500 Nm*

A more detailed insight is provided by the **individual contact stiffness components**, which reveal the redistribution of load among different tooth pairs. During the meshing transition, the stiffness contribution associated with the outgoing tooth pair progressively decreases and approaches zero, while the incoming tooth pair exhibits a complementary increase. Local stiffness values close to zero identify **regions where no effective mechanical interaction occurs between the tooth flanks**, despite geometric proximity. These regions can therefore be interpreted as **zero-contact-force regions**, in which contact is kinematically admissible but mechanically inactive.

$$k_c = \frac{\partial F_n}{\partial \delta_n} \qquad F_n = C\,\delta_n^{3/2} \Rightarrow k_c = \frac{3}{2} C\,\delta_n^{1/2} \tag{4}$$

*Equation 4: local mesh stiffness calculation*

The dynamic response of the system is obtained through direct time integration using the Newmark integration scheme. The rotational motion of the gears is handled by means of transformation matrices and by reordering the degrees of freedom at each meshing cycle, ensuring consistency of the contact conditions throughout the simulation.

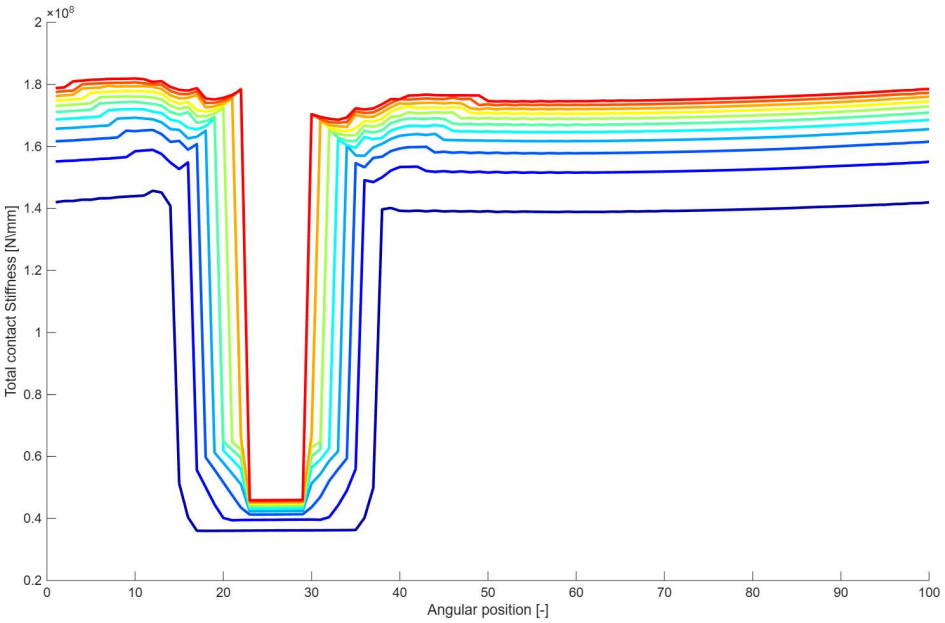


*Figure 3: Total Contact Stiffness map for torques from 10 to 500 Nm*

Additional nonlinear effects are also included in the model. Contact loss is modeled by removing the corresponding mesh stiffness contribution when separation occurs, while recontact events are treated as vibro-impacts, introducing a discontinuity in the relative velocity of the interacting bodies.

$$k_{TVMS}(\theta, T) = \sum_{j=1}^{N_c(\theta)} k_{c,j}(\theta, T) \quad (5)$$

*Equation 5: time-varying mesh stiffness*

The **total contact stiffness** exhibits a clearly periodic trend, reflecting the cyclic nature of the gear meshing process. A pronounced reduction in stiffness is observed within a limited angular interval, corresponding to the **transition between successive tooth pairs**. In this region, the number of teeth simultaneously in contact is reduced, leading to a temporary decrease in the global mesh stiffness. Nevertheless, the total stiffness does not collapse to zero, since at least one tooth pair remains engaged and additional elastic contributions arise from the structural compliance of the gear bodies and boundary conditions.

$$M_r\ddot{q} + C_r\dot{q} + K_r(\theta, T)q = f_{ext}(T) \quad (6)$$

*Equation 6: reduced-order dynamic system*

$$q_{n+1} = q_n + \Delta t \dot{q}_n + \Delta t^2 (\frac{1}{2} - \beta) \ddot{q}_n + \beta \Delta t^2 \ddot{q}_{n+1} \quad (7)$$

$$\dot{q}_{n+1} = \dot{q}_n + \Delta t (1 - \gamma) \ddot{q}_n + \gamma \Delta t \ddot{q}_{n+1} \quad (8)$$

*Equation 7-8: the Newmark-β system time-based equations*

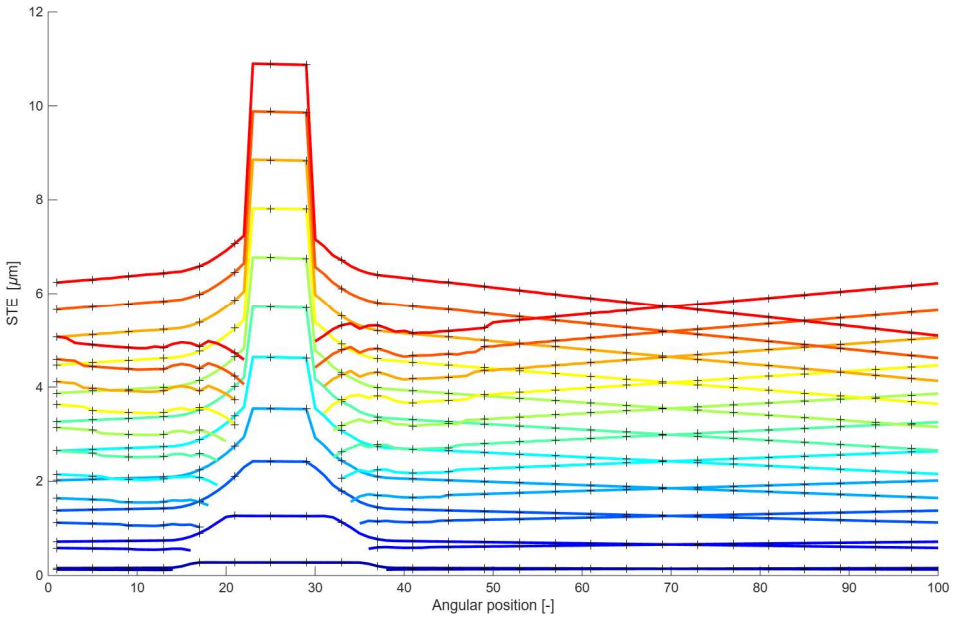


*Figure 4: Static Transmission Error for torque from 10 to 500 Nm*

The **static transmission error** shows a strong correlation with the contact stiffness evolution. A pronounced peak in STE is observed in the same angular interval where the contact stiffness reaches its minimum. This behavior is consistent with the inverse relationship between deformation and stiffness: under a given transmitted load, a reduction in mesh stiffness leads to increased elastic deflection and, consequently, to a higher transmission error. As the meshing process stabilizes and the number of active contacts increases, stiffness recovers and the STE decreases accordingly.

$$STE(\theta) = R_b(\theta_{out} - \theta_{in} \frac{Z_{in}}{Z_{out}}) \quad (9)$$

*Equation 9: static transmission error*

Overall, the combined analysis of contact stiffness, static transmission error highlights the strong interplay between contact mechanics, structural compliance, and numerical representation. The regions characterized by negligible contact forces play a key role in governing both the mechanical response of the gear pair and the structure of the finite element matrices, especially during tooth pair transitions.

# MODEL VALIDATION

The proposed gear dynamic model is validated through comparison with experimental data obtained from tests performed on steel spur gears. The main geometric and material parameters of the tested gears are reported in a dedicated table. Attention is paid to the influence of load-dependent effects, as the time-varying mesh stiffness (TVMS) is shown to vary with the applied torque, directly affecting the contact ratio and, consequently, the dynamic behavior of the system.

The validation process first focuses on the identification of the system's torsional natural frequency. The model predicts a fundamental torsional resonance at approximately 2650 Hz, which is in very good agreement with the experimental measurements.

$$\omega_n = \sqrt{\frac{k_{eq}}{J_{eq}}} \quad ; \quad f_n = \frac{1}{2\pi}\sqrt{\frac{k_{eq}}{J_{eq}}} \tag{10}$$

*Equation 10: torsional natural frequency*

Damping is introduced through an equivalent viscous formulation and calibrated using the logarithmic decrement method, resulting in a damping ratio of about 8%, consistent with the experimental observations. From a computational standpoint, the performance of the proposed approach is also assessed.

$$\delta = ln\left(\frac{x(t)}{x(t+T_d)}\right) \tag{11}$$

*Equation 11: damping ratio with decrement method*

A speed sweep from 900 to 4100 rpm is simulated, requiring approximately six-million-time steps and less than 20 hours of computation on a single processor, without any form of parallelization. Despite the demanding nature of the analysis, the computational cost remains significantly lower than that associated with full finite element simulations offering comparable accuracy.

The model can accurately reproduce several nonlinear dynamic phenomena observed experimentally. In particular, the primary torsional resonance occurring around 2700 Hz is captured, including the characteristic hysteretic jumps during sweep-up and sweep-down maneuvers. Additional harmonic resonances corresponding to subharmonic excitations at $\omega_n/2$ and $\omega_n/3$ are also correctly predicted.

Both resonance frequencies and vibration amplitudes show good agreement with the experimental data, with the only notable discrepancy being a slight underestimation of the third harmonic response.

Finally, the analysis of the tooth contact forces provides further insight into the nonlinear behavior of the system. A softening effect is observed near resonance conditions, which is directly associated with partial or total contact loss between the gear teeth. This confirms the importance of accurately modeling contact loss and recovery to capture the correct dynamic response of geared systems.

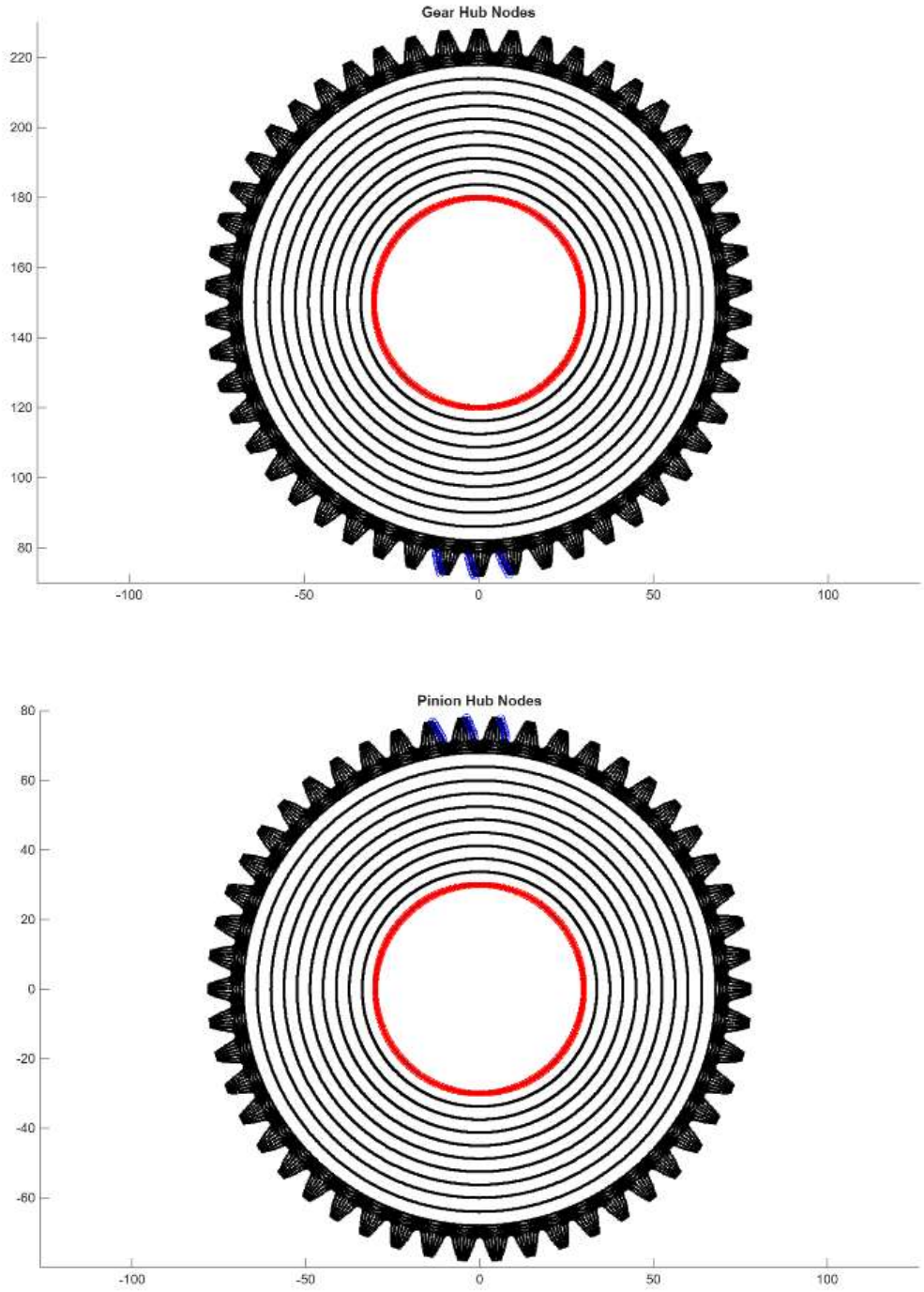


*Figure 5-6: Finite Element Representation of Gear and Pinion hub*

The representations provide a comprehensive view of the spatial distribution of nodes used to describe both the structural core of the hub and the external toothed rim, which is directly involved in load transmission and contact interaction.

The **outer ring of nodes** corresponds to the toothed portion of the gear, where mechanical engagement with the mating component occurs. This region is discretized with increased nodal density to accurately capture local stiffness variations, stress gradients, and contact-related phenomena that are critical for both static and dynamic analyses. Internally, the hub is discretized using **multiple concentric rings of nodes**, forming a structured and axisymmetric nodal pattern. This arrangement ensures a consistent representation of mass distribution, radial and torsional stiffness and deformation modes associated with the hub body.

Such a nodal configuration is particularly well suited for modal analyses and reduced-order modeling, as it preserves the geometric symmetry and mechanical continuity of the component while maintaining numerical efficiency. A **specific annular region is highlighted**, indicating a subset of nodes that are explicitly identified for further analytical treatment.

These nodes are associated either to mechanically critical interface, transition zone between subcomponents or a functional element subjected to relative motion or localized compliance. This highlighted region is used to **define the contact or coupling interface**, from which contact forces, stiffness contributions, or constraint relations are extracted. Isolating this subset of nodes allows for a clear separation between the structural degrees of freedom of the hub and those involved in contact interactions.

The nodal configuration is presented in the **global Cartesian reference frame**, with the X–Y coordinates representing the spatial position of each finite element node. The coordinate range reflects the actual geometric dimensions of the component and provides a consistent basis for defining boundary conditions, constructing transformation matrices and assembling global stiffness and mass matrices.

This separation is fundamental for the subsequent development of the contact model, the evaluation of mesh stiffness, and the formulation of reduced-order dynamic models, ensuring both numerical stability and physical consistency of the simulation results.

# REDUCED-ORDER MODELING OF THE GEAR PAIR

In order to drastically reduce the number of degrees of freedom (DoFs) of the finite element model while preserving a high level of accuracy, a Craig–Bampton Component Mode Synthesis (CB-CMS) approach is adopted. Each gear, namely the pinion and the wheel, is reduced independently to maintain modeling flexibility and generality.

A limited number of key nodes are selected in the reduction process. Contact stiffness nodes are defined at the meshing interfaces, where gear engagement occurs and where the main sources of nonlinearity are introduced. Additional auxiliary observed nodes are selected using the MoGeSeC criterion to improve modal fidelity and ensure accurate representation of the structural dynamics. Virtual central nodes are also introduced to represent the shaft center; these nodes are used to apply the input torque and to extract global dynamic quantities.

$$\boldsymbol{MAC}(\boldsymbol{\phi_i}, \boldsymbol{\psi_j}) = \frac{\left|\boldsymbol{\phi i_i^T \psi_j}^{\boldsymbol{2}}\right|}{(\boldsymbol{\phi_i^T \phi_i})(\boldsymbol{\psi_j^T \psi_j})} \tag{12}$$

*Equation 12: Modal Assurance Criterion*

No geometric simplifications are introduced, and the full flexibility of the gear bodies is retained in the reduced models. When compared with the full finite element model, the reduction accuracy is assessed by imposing a maximum relative error below 0.05% and a Modal Assurance Criterion (MAC) exceeding 88%, demonstrating excellent agreement. As a result, the number of DoFs is reduced from approximately 270,000 in the full FEM to only 229 DoFs per gear, while preserving an almost identical dynamic behavior and achieving a substantial reduction in computational time.

Gear meshing is inherently periodic, and the actual rolling motion is discretized into $N$ angular sub-intervals. At each step, the pinion and the wheel are rotated by small angular increments ($\Delta\theta_{\mathrm{p}}$ and $\Delta\theta g$, respectively), and the reduced mass and stiffness matrices are updated to reflect the new relative position. The contact stiffness, represented by the time-varying mesh stiffness (TVMS), is updated according to both the angular position and the instantaneous load. Time integration of the equations of motion is performed using the Newmark integration scheme, chosen for its stability and accuracy in nonlinear dynamic analyses.

$$\boldsymbol{\theta_p^{(i)} = \theta_p^{(i-1)} + \Delta\theta_p}$$

$$\boldsymbol{\theta_g^{(i)} = \theta_g^{(i-1)} + \Delta\theta_g} \tag{13}$$

*Equation 13: Small Angular Increments for pinion and gear*

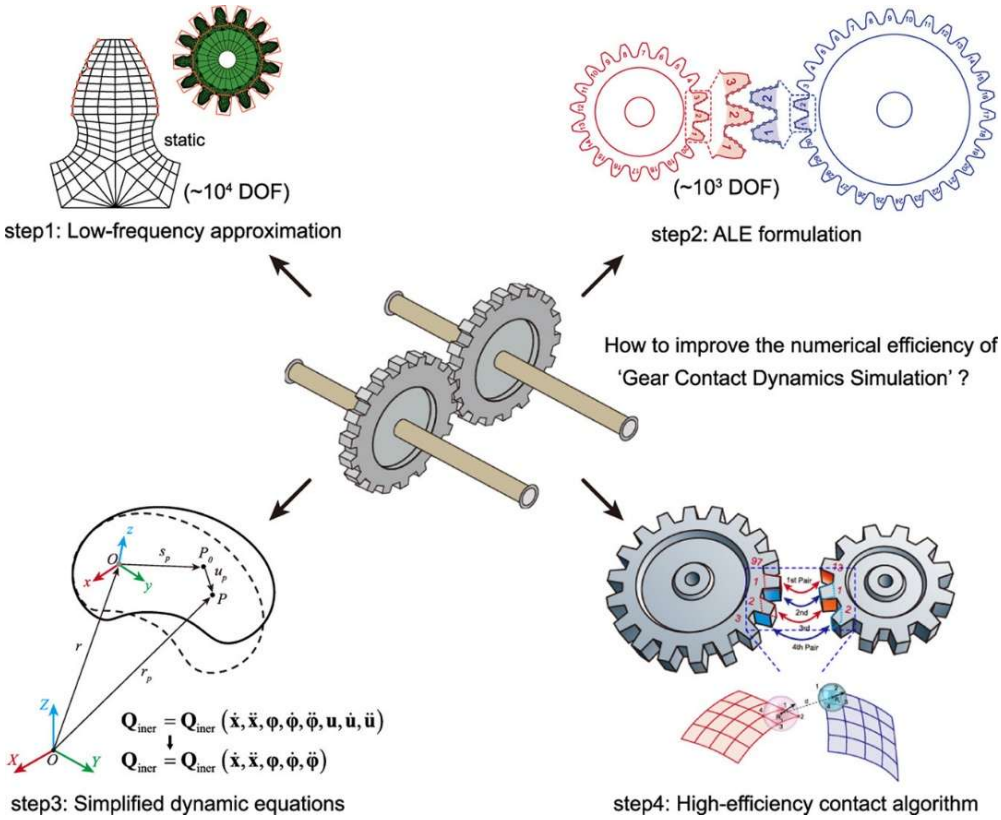


*Figure 7: Reduced Model step representation of Gear Contact*

After each complete meshing cycle, the degrees of freedom are reordered to restore the initial reference configuration, allowing continuous simulation of the rolling process over multiple revolutions. In the event of contact loss, the corresponding stiffness contribution is deactivated by setting the contact indicator to zero. When contact is re-established, the interaction is modeled as a vibro-impact, introducing a velocity discontinuity governed by a restitution coefficient.

$$\chi = \begin{cases} \mathbf{1}\ \boldsymbol{if}\ \boldsymbol{\delta_n > 0} \\ \mathbf{0}\ \boldsymbol{if}\ \ \boldsymbol{\delta_n \leq 0} \end{cases} \tag{14}$$

*Equation 14: Contact Loss effect*

This modeling strategy enables the accurate reproduction of key nonlinear dynamic phenomena observed in real gear systems, including resonances, hysteretic jumps, and partial or total loss of tooth contact.

$$\boldsymbol{DTE = R_b\left(\theta_p - \theta_g \frac{Z_p}{Z_g}\right)} \tag{15}$$

*Equation 15: Dynamic Transmission Error*

# TIME-VARYING MESH STIFFNESS & DYNAMIC SIMULATION

The time-varying mesh stiffness during tooth rolling is precomputed through a series of static finite element analyses performed at different torque levels. The resulting stiffness values are stored in a TVMS map $k_c(z, L)$, which depends on the instantaneous angular position $z$, corresponding to the contact point along the line of action, and on the applied load level $L$.

During the dynamic simulation, the TVMS is updated at each angular step according to the instantaneous load. Although contact stiffness is modeled as linear at each time step, its value depends on the load, thereby introducing an additional global nonlinearity into the system. Variations in the contact ratio, such as single-tooth and double-tooth contact regions, are automatically accounted for through the TVMS formulation. This approach eliminates the need to recompute the finite element contact problem at every time step, leading to a significant reduction in computational cost.

The dynamic response is computed in the time domain using direct Newmark integration, selected for its stability and accuracy in nonlinear analyses. At each time step, the reduced mass, stiffness, and damping matrices $\mathbf{M}_r$, $\mathbf{K}_r$, and $\mathbf{C}_r$ are updated according to the current angular position. The time- and load-dependent contact stiffness matrix $\mathbf{K}_c(z, L)$ is then included in the system equations.

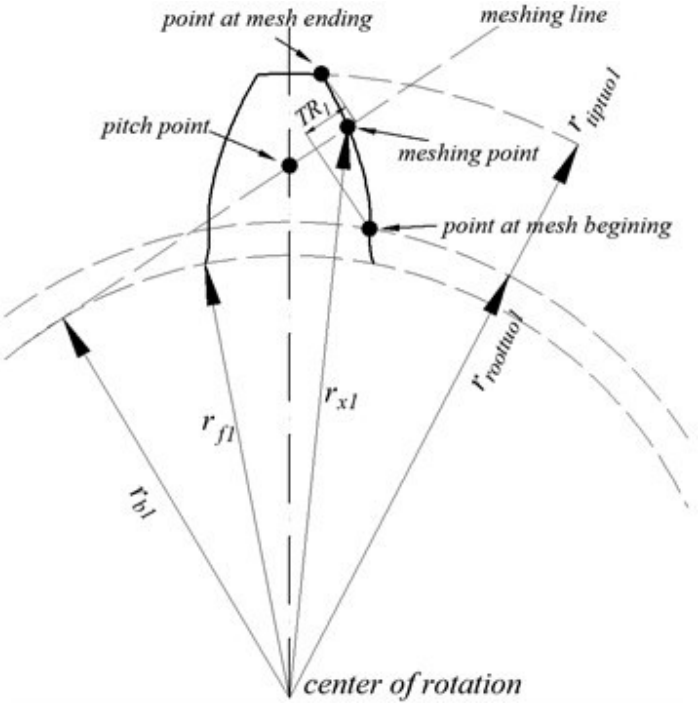


*Figure 5: Gear Scheme Mesh*

At each integration step, the following quantities are computed for all reduced degrees of freedom: displacements, velocities, and accelerations. After each complete rotation, corresponding to one full

meshing cycle, the degrees of freedom are reordered to restore the initial reference configuration and to ensure continuity of motion over successive cycles.

$$\boldsymbol{F_n = k_c(z, L)\delta_n} \tag{16}$$

*Equation 16: normal contact forces*

Contact nonlinearities are handled by monitoring the normal contact forces at each meshing element. When the normal force becomes tensile, contact loss is assumed and the corresponding stiffness contribution is deactivated. Upon recontact, the interaction is modeled as a vibro-impact, introducing a velocity discontinuity governed by a restitution coefficient $e$.

# TOOTH CONTACT IN THE REDUCED MODEL

In a full finite element model, the contact between gear teeth is computed in a continuous and fully geometric manner. Contact nodes are either coincidence or perfectly projected along the line of action, ensuring an exact spatial correspondence between the interacting tooth surfaces throughout the meshing cycle.

In the present reduced-order model, the contact representation is simplified to improve computational efficiency. The tooth profiles are described in an idealized manner, using analytical curves or discretized spline representations. Contact points are therefore identified numerically or geometrically as approximate intersections between the two mating surfaces.

$$x_p(z) \neq x_g(z) \tag{17}$$

*Equation 17: coordinate along the line of action*

Therefore, the contact points associated with the pinion and the gear do not coincide exactly in space. This results in a small spatial offset between the vectors representing the contact forces (highlighted, for example, by the red and blue bars in the figure), even though they are intended to represent the same physical contact location along the line of action.

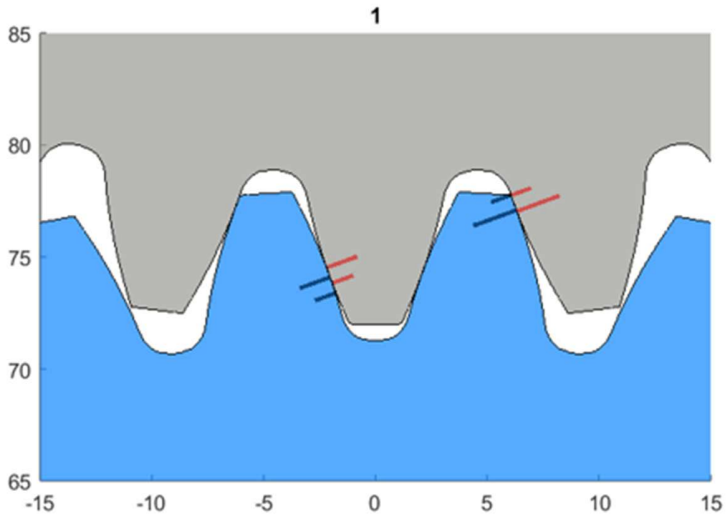


*Figure 7: Finite Element simulation of two mechanical profiles in contact*

It is important to emphasize that this mismatch is purely graphical or numerical in nature and does not represent a physical separation or modeling inconsistency. The offset does not affect the computation of the normal contact force, the time-varying mesh stiffness, or the resulting dynamic response of the system. The actual kinematic and dynamic interactions between the gears are correctly enforced through the contact stiffness formulation and the projection along the line of action.

The image shows the evolution of the tooth contact during the meshing cycle of a spur gear pair. The pinion and the gear rotate continuously, and the contact between the mating tooth profiles progresses along the line of action as the rolling motion develops.

$$\boldsymbol{\delta_n = (u_p - u_g) \cdot n_{LOA}} \quad \textbf{(18)}$$

*Equation 18: relative displacement*

The tooth profiles are represented in a simplified, idealized form, and the instantaneous contact locations are highlighted by force vectors acting on each gear. These vectors, depicted with different colors (e.g., red for one gear and blue for the mating gear), indicate the normal contact forces applied at the corresponding contact points on each tooth flank.

Due to the simplified numerical representation of the tooth geometry and the independent determination of contact points on each gear, the force vectors associated with the pinion and the gear do not appear to be perfectly coincident in space. A small apparent offset between the vectors can be observed throughout the animation. This offset varies slightly during the meshing cycle as the contact point moves along the tooth profiles.

Different degrees were illustrated, and the continuous transfer of load between teeth and the alternation between single-tooth and double-tooth contact regions. It provides a visual representation of the rolling process and contact force evolution, while highlighting the numerical nature of the contact point definition in the reduced-order model.

# STATIC VERIFICATION OF THE CONTACT MODEL

The model was first tested by considering the contact points shown in the figure, for which all nodal matrices are known, to perform static verification analyses. The results allow a preliminary assessment of the correctness of the contact formulation and of the stiffness distribution along the meshing cycle.

As shown in the figures, regions where the contact forces are zero indicate the absence of mechanical interaction between the mating tooth profiles. These points correspond to separation zones or transition regions between one pair of teeth and the next, which are typical of the transition from single-tooth to double-tooth contact.

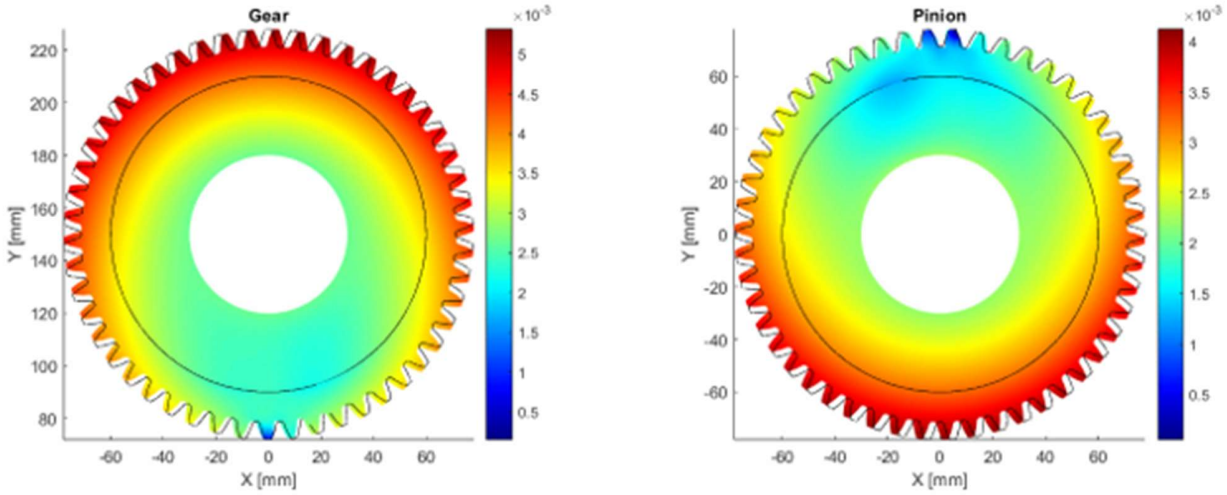


*Figure 8: Modal Analysis Radial Coupled Map*

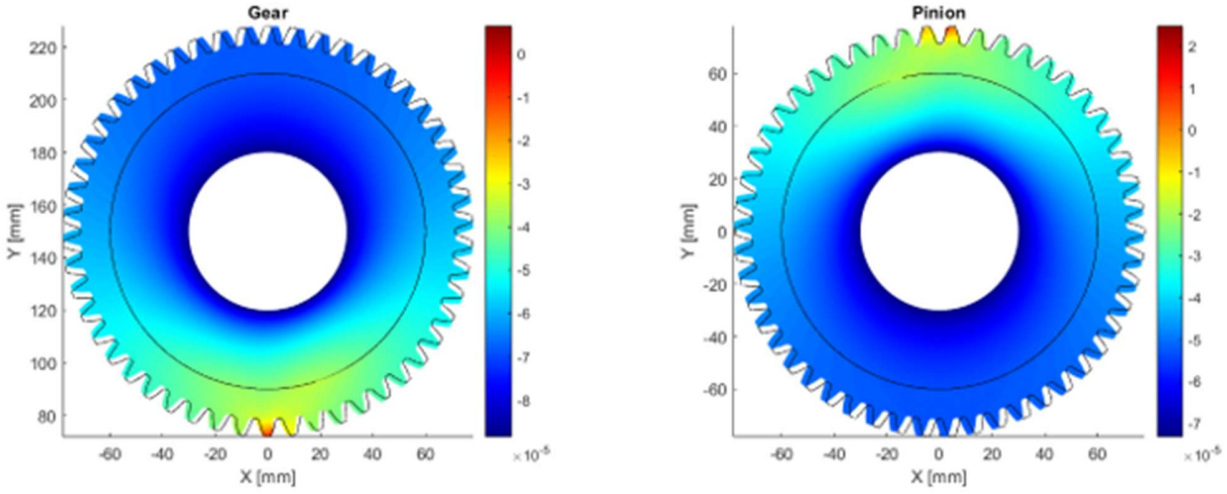


*Figure 9: Modal Analysis Radial Coupled Map*

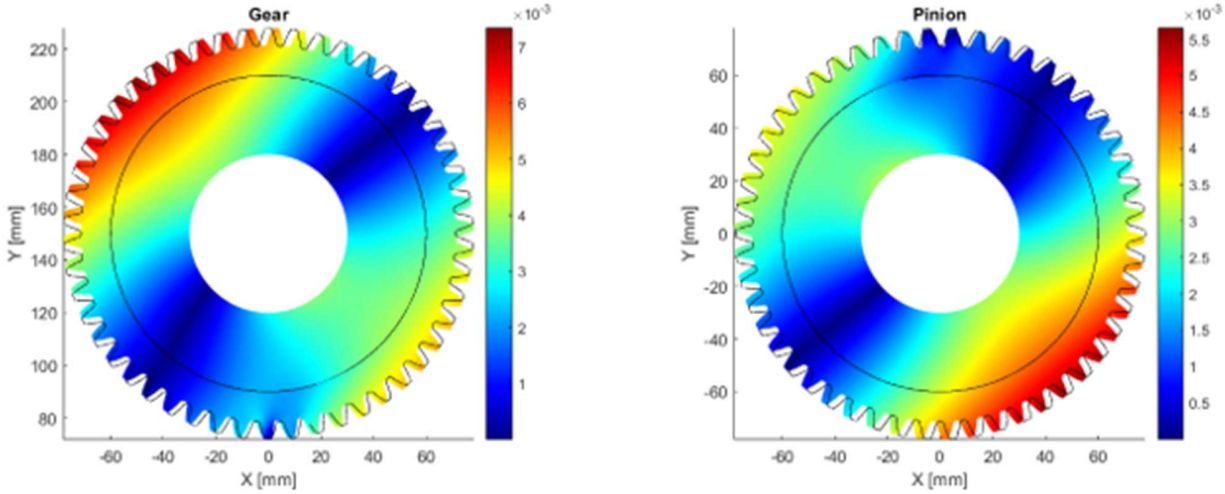


*Figure 10: Modal Analysis Radial Coupled Map*

In simplified gear models, similar effects may also arise from numerical approximations associated with the discretization of the contact interface. However, in the present formulation, the observed zero-force regions are primarily related to the actual kinematics of the meshing process and to the load-dependent evolution of the contact conditions.

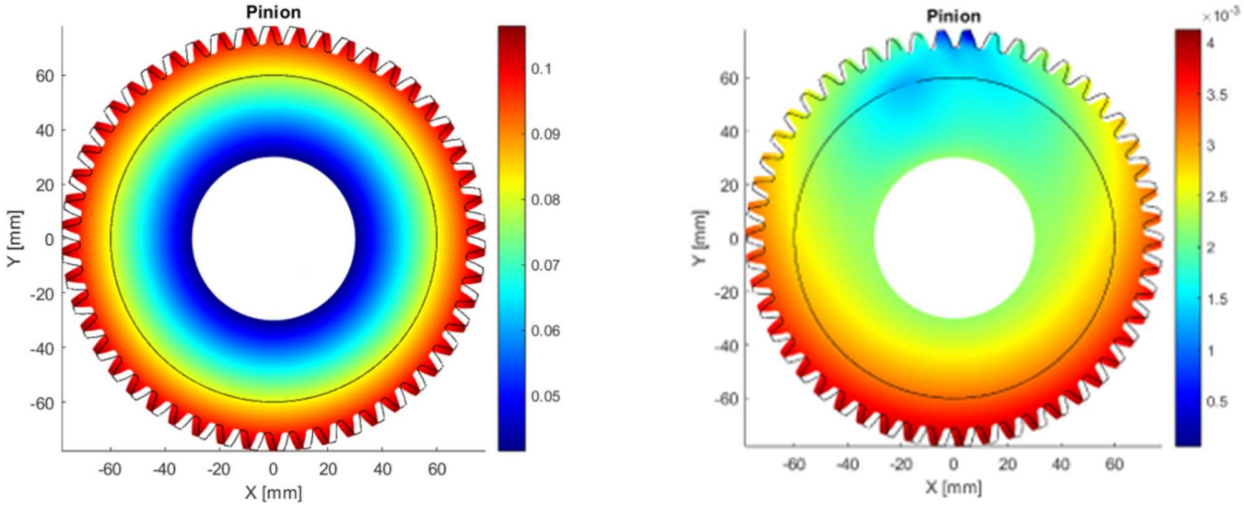


*Figure 6: Error in the Static Analysis Radial Map*

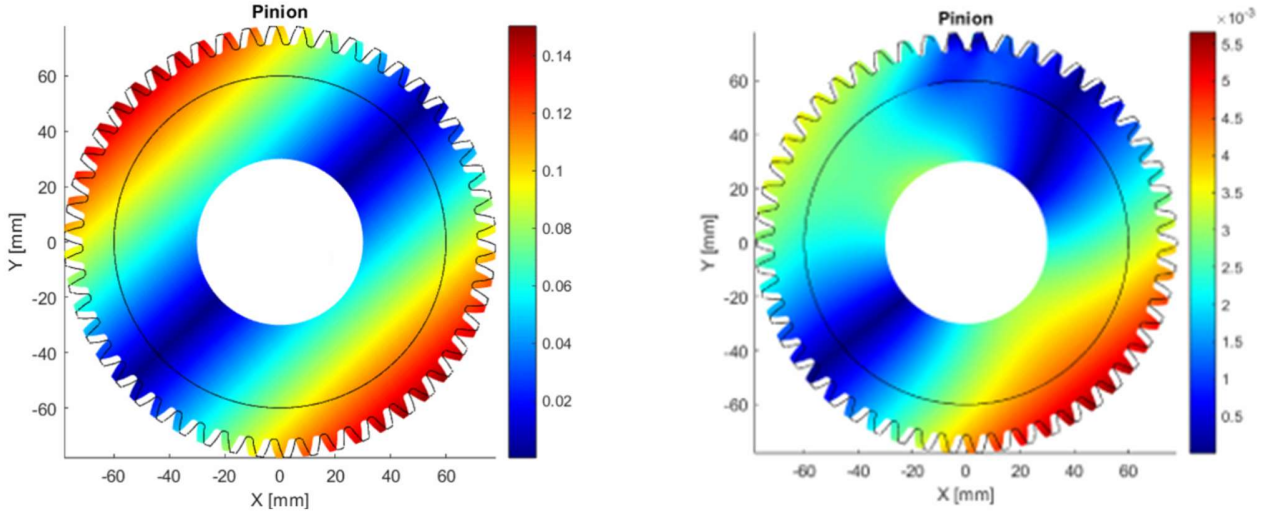


*Figure 7: Error in the Static Analysis Circular Map*

As contact initiates, the stress progressively increases in the region where the tooth surfaces come into engagement. Conversely, the stress gradually decreases to zero as the tooth pair disengages. During phases in which two tooth pairs simultaneously share the transmitted load (double-tooth contact), the stress maps typically exhibit two distinct stress peaks, associated with the two active contact zones, separated by an intermediate region with nearly neutral stress levels.

At points where the contact force vanishes, the absence of contact pressure implies that the stress state is either purely residual elastic stress or effectively null. This behavior is consistent with the expected physical response of gear teeth during rolling contact and confirms the capability of the model to correctly capture contact transitions and load redistribution effects.

# ZERO-CONTACT-FORCE REGIONS IN MODAL ANALYSIS

Regions in which the contact forces are equal to zero indicate the absence of mechanical interaction between the mating tooth profiles. These regions are also observed in modal analysis and exhibit a behavior fully consistent with that previously identified in the static simulations. The recurrence of the same contact patterns across different types of analyses suggests that this phenomenon is intrinsic to the contact formulation and to the meshing kinematics, rather than being an artifact introduced by the dynamic or modal solution procedure.

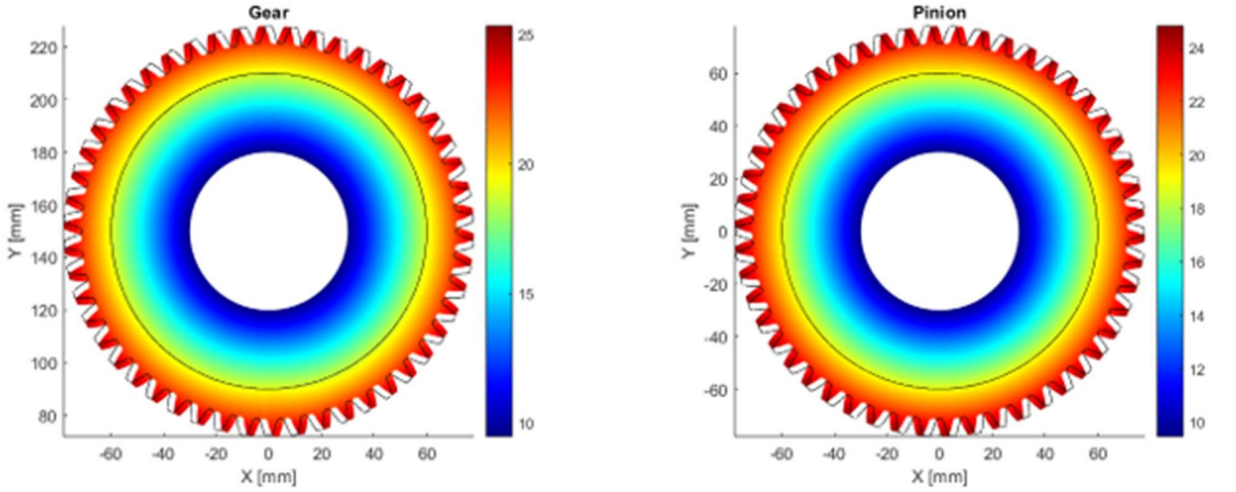


*Figure 11: Modal Analysis Radial Coupled Map*

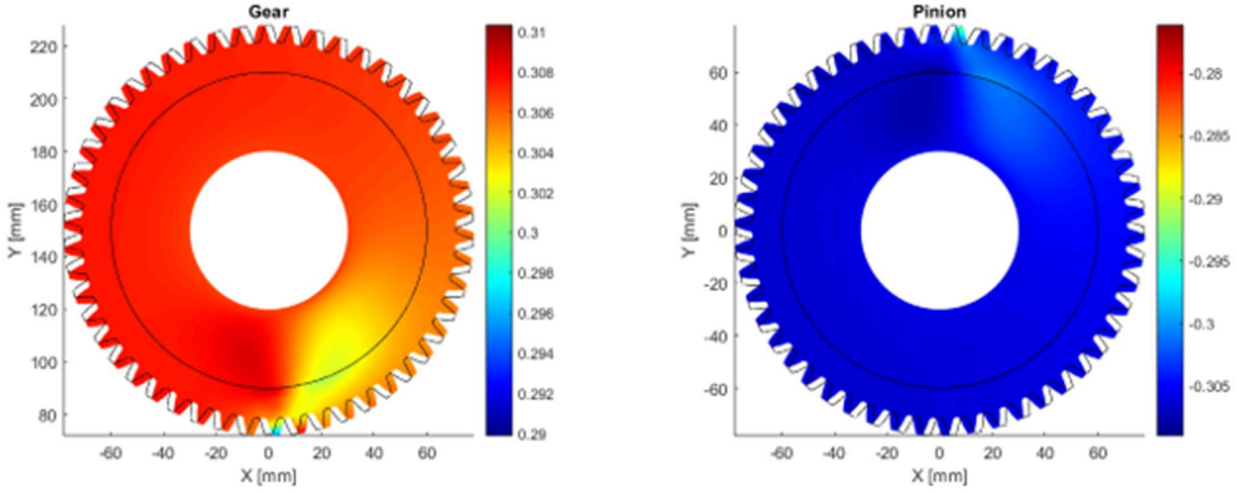


*Figure 12: Modal Analysis Tangential Coupled Map*

In the modal domain, zero-contact-force regions typically arise in correspondence with angular positions where the meshing teeth are either disengaged or undergoing a transition between successive tooth pairs. These zones are therefore representative of the natural evolution of the

contact conditions during gear rotation and are closely related to variations in the contact ratio, such as the transition between single-tooth and double-tooth contact phases.

From a numerical perspective, it is important to note that in simplified gear models similar effects may also be amplified or partially induced by approximations introduced in the contact discretization. In particular, the use of a limited number of contact nodes or simplified kinematic assumptions can lead to localized regions where the contact stiffness is effectively reduced or temporarily deactivated. However, in the present formulation, the agreement between static and modal results indicates that the observed zero-force regions primarily reflect the physical contact behavior rather than numerical artifacts.

The consistency of the contact force distribution between static and modal analyses provides additional validation of the reduced-order model and confirms the robustness of the contact representation. This ensures that the modal properties of the system are computed on a physically meaningful contact configuration, which is essential for accurately predicting resonance phenomena, mode coupling, and nonlinear dynamic responses in subsequent time-domain simulations.

At locations where the contact force becomes zero, no contact pressure is transmitted between the mating tooth surfaces, and consequently no local contact stress or deformation develops. In the finite element stress maps, these regions appear as areas with stress values close to zero, typically represented by dark blue colors in standard FEM color scales. The presence of such regions is therefore a clear indicator of the absence of mechanical interaction between the gear teeth at those locations.

From a physical standpoint, these zones can be associated with different phases of the meshing process. They may correspond to portions of the tooth flank that are not engaged in contact, to load release regions occurring during the transition between two successive tooth pairs, or to areas of partial separation induced by local flexibility effects or slight misalignments of the gear bodies.

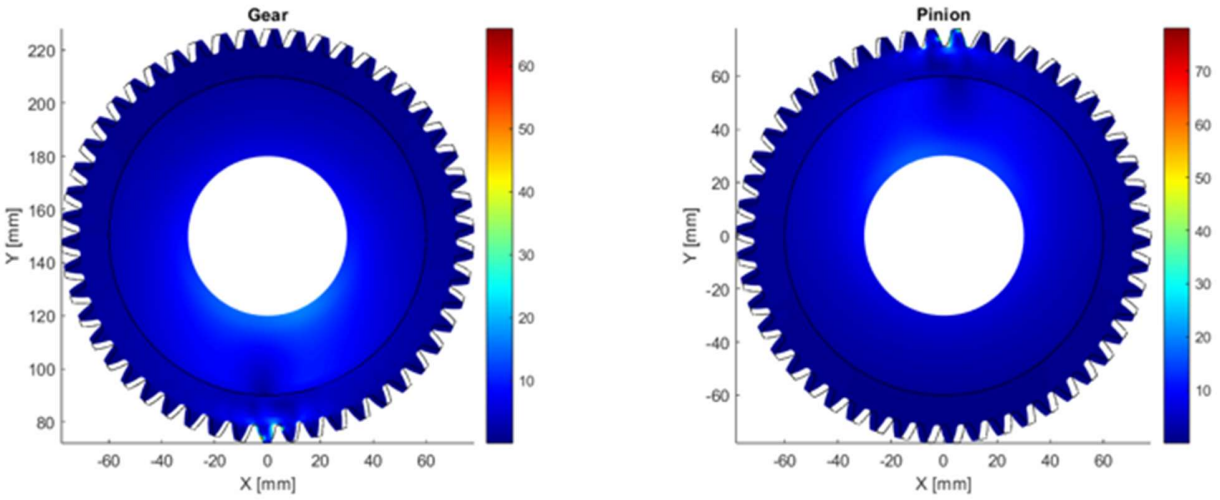


*Figure 13: Modal Analysis Von Mises Coupled Map*

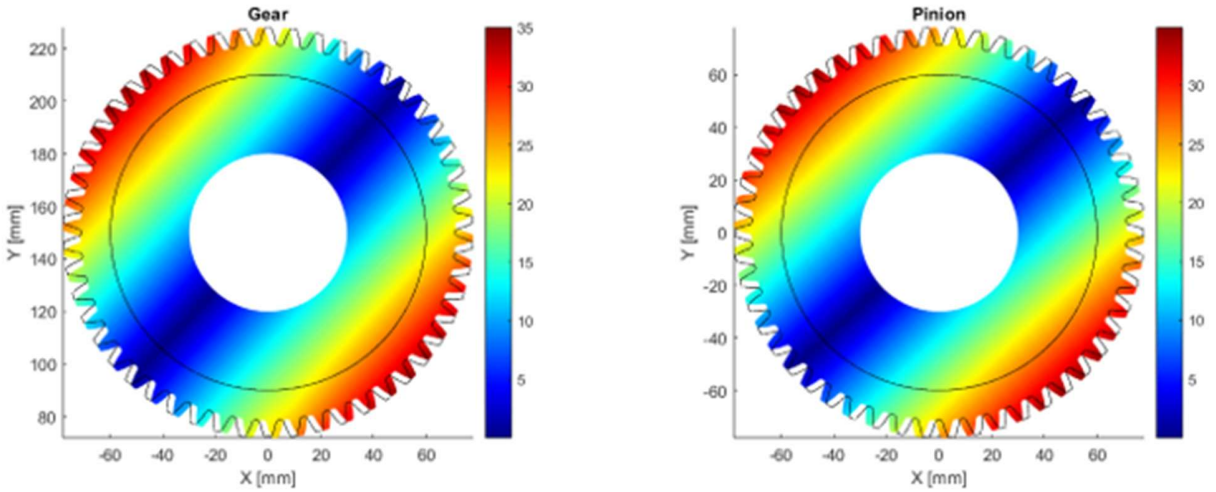


*Figure 14: Modal Analysis Circular Coupled Map*

As the meshing cycle evolves, the contact stress gradually increases in the regions where contact is established and progressively decreases to zero as the tooth pair disengages.

During operating conditions in which two tooth pairs simultaneously share the transmitted load, the stress maps typically exhibit two distinct stress peaks associated with the active contact zones, separated by intermediate regions characterized by very low or nearly zero stress levels. This behavior reflects the redistribution of the load between the engaged tooth pairs and is consistent with the expected physical response of spur gear systems.

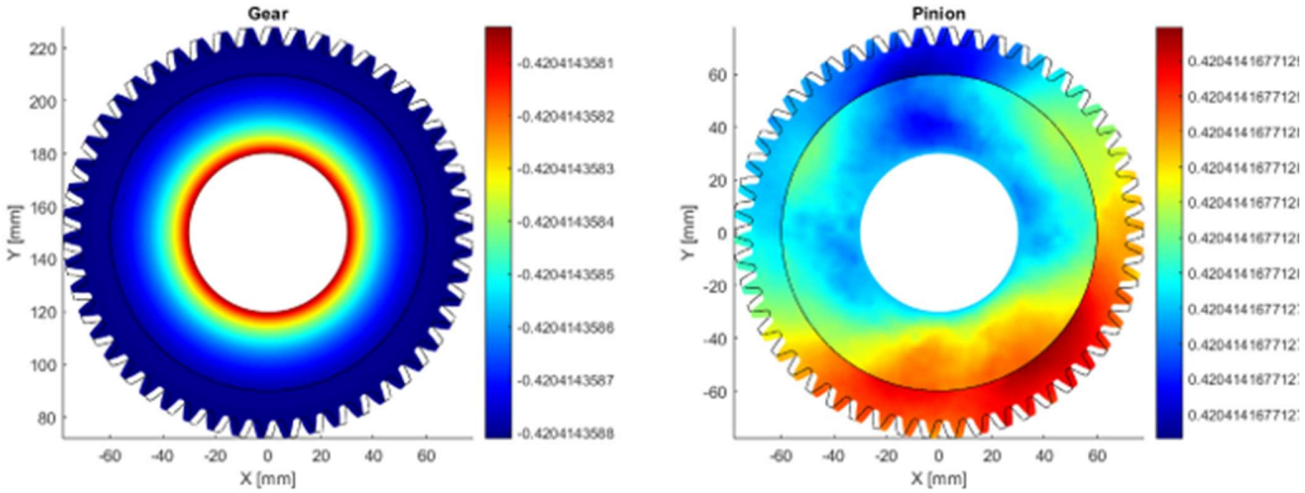


*Figure 18: Modal Analysis Tangential Uncoupled Map*

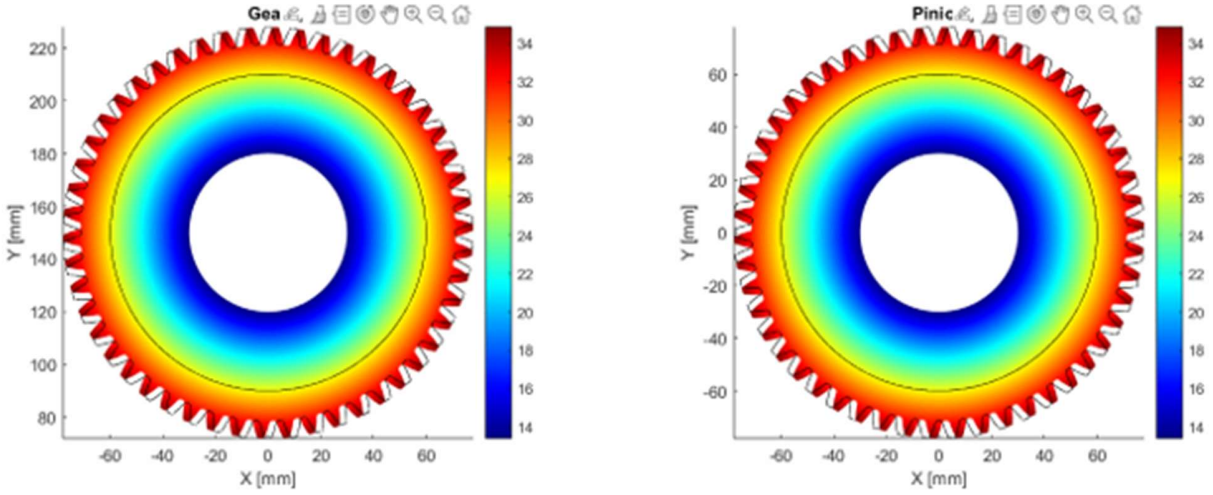


*Figure 19: Modal Analysis Radial Uncoupled Map*

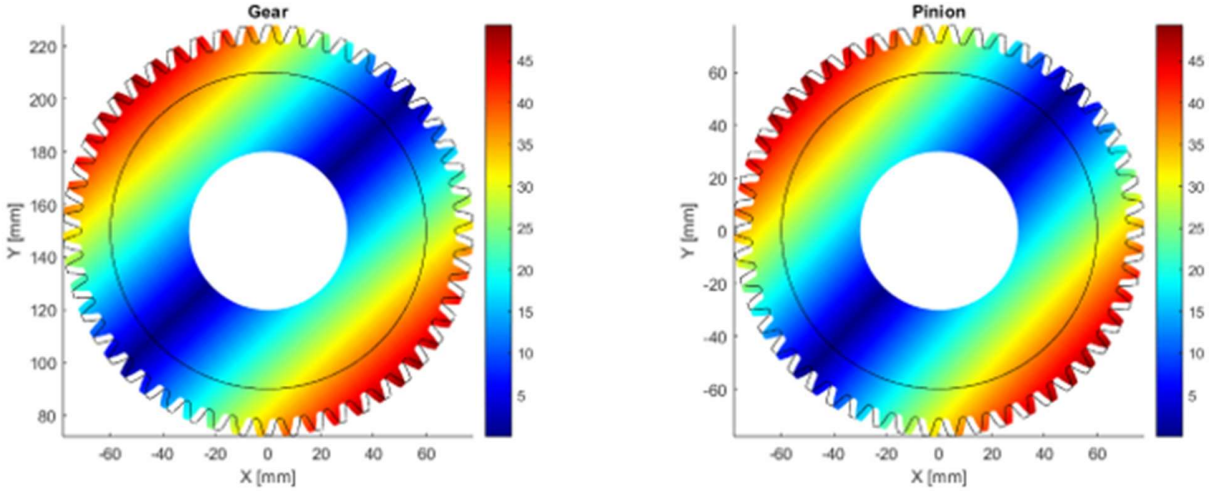


*Figure 110: Modal Analysis Circular Uncoupled Map*

The overall behavior observed in these regions is fully analogous to that obtained in the static analyses, indicating that the same contact mechanisms govern both static and dynamic conditions. This consistency confirms the reliability of the contact modeling approach and supports the validity of the reduced-order formulation in accurately capturing contact transitions and load transfer phenomena during gear meshing.

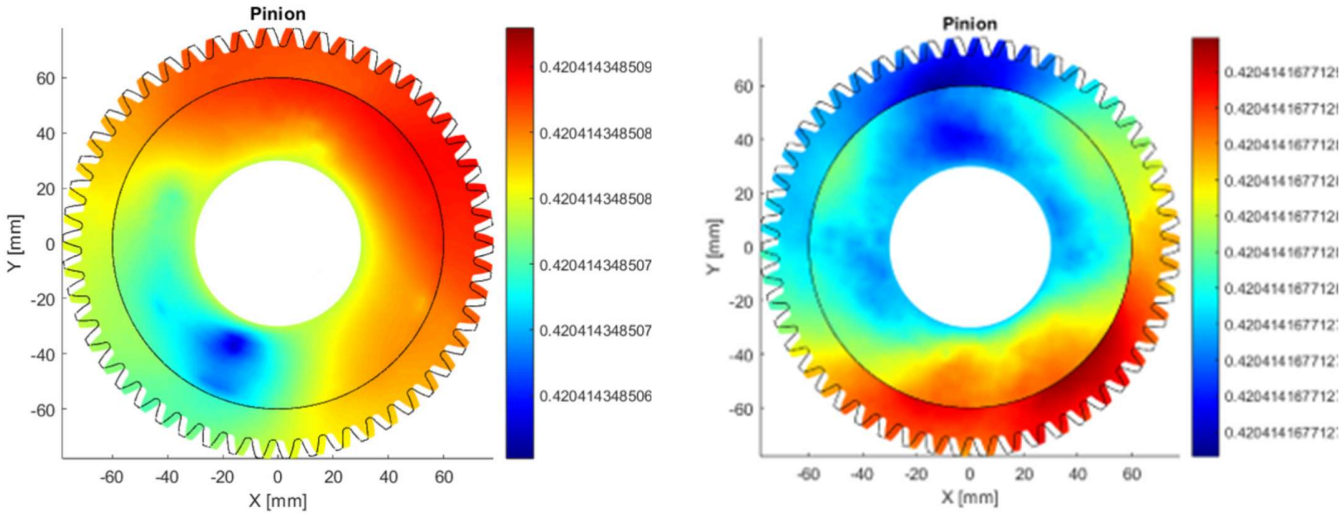


*Figure 11: Errors in Modal Uncoupled Tangential Map*

# NATURAL FREQUENCIES

Each curve represents a reduced natural frequency evaluated for a different angular position of the tooth in contact. The small oscillations observed along the curves indicate a weak dependence of natural frequencies on the angular configuration of the meshing gears. This behavior is mainly associated with local variations in contact stiffness and in the distribution of the effective mass as the contact point moves along the tooth flank.

$$(\boldsymbol{K_r}(\boldsymbol{z}) - \boldsymbol{\omega_i^2 M_r})\boldsymbol{\phi_i} = \mathbf{0} \quad \textbf{(19)}$$

*Equation 19: reduced dynamic system*

When the meshing condition transitions from double-tooth to single-tooth contact, the local stiffness of the system decreases, leading to a slight reduction in the corresponding natural frequencies. This trend is consistently captured across the analyzed angular positions and reflects the expected physical response of the gear pair during the meshing cycle.

At angular positions of approximately 5–10 degrees, a more pronounced drop can be observed in some of the frequency curves, particularly in the range around 3500–4000 Hz. This irregular or anomalous behavior suggests a temporary reduction in the overall meshing stiffness, which is likely associated with the transition between two successive tooth pairs in contact. Additional contributing factors may include local geometric asymmetries or slight misalignments in the gear wheel, as well as numerical discontinuities introduced during the regeneration of the reduced-order model when rotating from one tooth to the next.

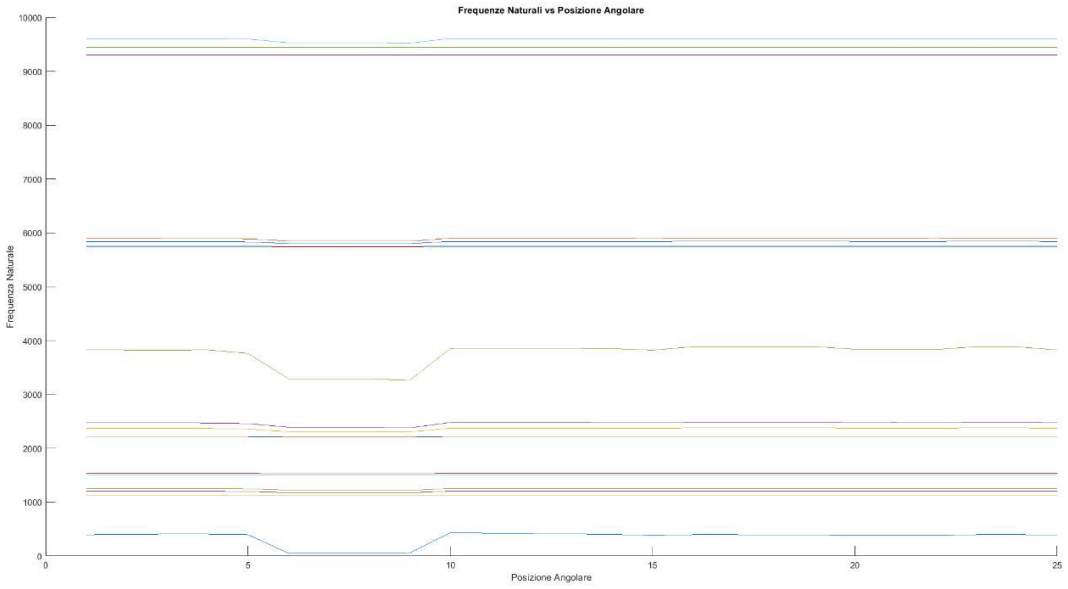


*Figure 12: Natural Frequencies Coupled Gears*

The remaining frequency curves remain relatively stable throughout the meshing cycle, confirming that the observed variation primarily affects specific flexural modes that are more sensitive to the contact conditions. This selective sensitivity further supports the physical consistency of the results and indicates that the reduced-order model can capture localized stiffness variations without introducing spurious global effects.

Regions in which the contact forces are equal to zero indicate the absence of mechanical interaction between the mating tooth profiles. As discussed in the previous analyses of normal contact forces and stress distributions, these regions are associated with tooth disengagement phases or with transitions between successive tooth pairs during the meshing cycle.

When considering the tangential force components, a different behavior is observed compared to the normal contact forces previously analyzed. Variations are detected only on the pinion side, while the corresponding tangential forces on the mating gear remain essentially constant. This behavior can be explained by the way the torque is applied and transmitted through the system: the pinion is the driven component and directly reflects variations induced by local contact conditions, stiffness changes, and dynamic effects, whereas the wheel experiences a smoother and more uniform load transfer.

$$f_i \propto \sqrt{\frac{k_{eff}}{m_{eff}}} \tag{20}$$

*Equation 20: natural frequency - stiffness-to-mass ratio relation*

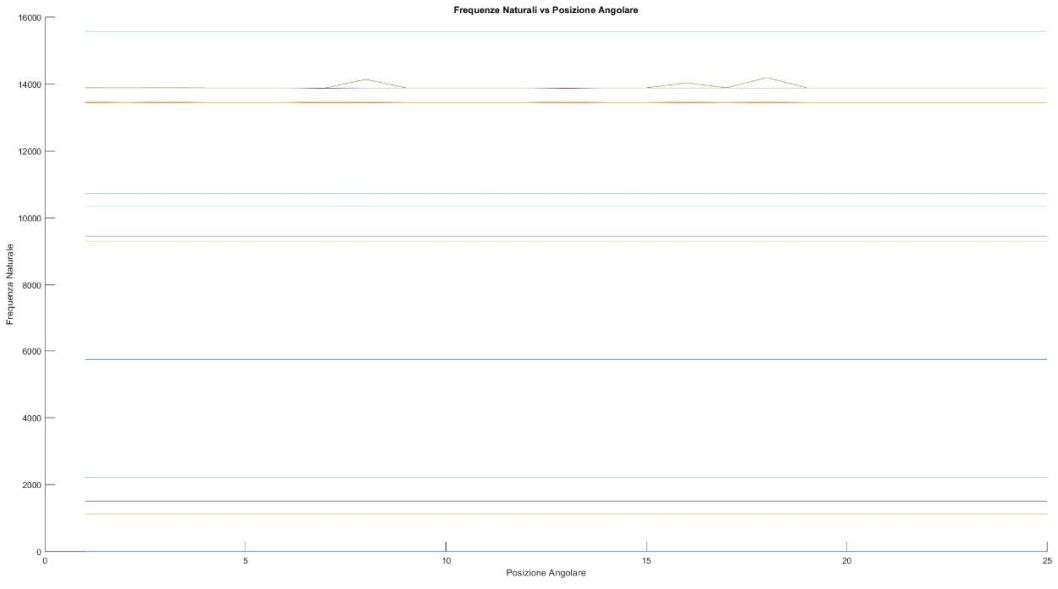


*Figure 13: Natural Frequencies Uncoupled Gears*

In contrast to the coupled normal contact forces discussed above, which are strongly influenced by contact loss, re-engagement, and changes in the contact ratio, the tangential forces exhibit reduced sensitivity to these local phenomena. Even in correspondence with regions where the normal contact force vanishes, the tangential force on the pinion does not show abrupt discontinuities but rather maintains a nearly constant mean value with limited fluctuations.

This comparison highlights the different physical roles played by normal and tangential contact forces in gear dynamics. While the normal force is directly affected by contact conditions and local stiffness variations—leading to zero-force regions, stress-free zones, and nonlinear effects—the tangential force primarily reflects the global torque transmission and is therefore less sensitive to localized contact phenomena. The consistency between these observations and the previously discussed coupled contact-force behavior further confirms the physical coherence of the proposed modeling approach.

# THE APPLICATION OF RBE3

The figure illustrates the contact modeling strategy adopted for the gear pair at a given angular position. For each angular configuration, the contact formulation is applied for each finite element slice (five slices along the face width) and for each potentially engaged tooth, typically involving two to four teeth depending on the contact ratio.

The tooth contact is represented in a two-dimensional view and must be consistently defined for each FEM slice. On both the pinion and the gear wheel sides, a set of surface nodes belonging to the tooth flank is connected to a single master contact node through RBE3 elements. These RBE3 connections distribute the kinematic influence of the master node to the surrounding slave nodes without introducing artificial stiffness into the system.

The master contact nodes of the pinion and the wheel are connected through a spring element representing the contact stiffness. This stiffness corresponds to the time-varying mesh stiffness and is defined as $k_c/5$ for each slice, so that the total mesh stiffness is correctly recovered by summing the contributions of all slices. The spring is aligned along the local line of action and updated according to the instantaneous angular position and load level.

The coordinates of the pinion contact node are computed from the contact normal formulation, depending on the angular position. At each step, the two master nodes of the pinion and the wheel coincident in space, ensuring a physically consistent representation of the contact kinematics during rolling.

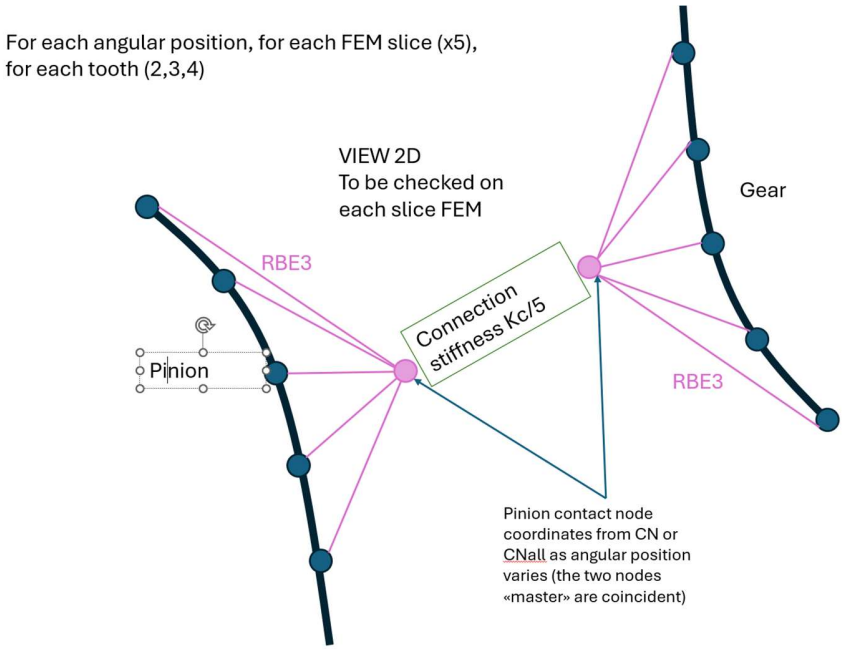


*Figure 14: RBE3 Functionality Scheme*

The use of RBE3 elements is a crucial aspect of the proposed modeling strategy. Unlike RBE2 elements, which impose rigid kinematic constraints and introduce artificial stiffness, RBE3 elements perform a weighted interpolation of displacements between the master and slave nodes without adding stiffness or mass to the system. As a result, forces are correctly transferred while preserving the flexibility of the connected structure.

From a theoretical standpoint, RBE3 elements enforce compatibility in a weak sense, distributing the motion of the master node to the surrounding slave nodes based on predefined weighting coefficients. This makes them particularly suitable for contact modeling and reduced-order formulations, where preserving the correct dynamic behavior is essential.

$$\boldsymbol{k_c} = \sum_{\boldsymbol{i=1}}^{\boldsymbol{N_s}} \boldsymbol{k_{slice,i}} \tag{21}$$

*Equation 21: total mesh stiffness*

In the present application, RBE3 elements are used to avoid the occurrence of numerical singularities or so-called "machine zeros" in the system matrices. If contact stiffness were applied directly between single nodes without a proper kinematic distribution, localized constraints could lead to ill-conditioned stiffness matrices, artificial local modes, spurious zero or near-zero eigenvalues. These numerical issues would, in turn, corrupt the computation of the natural frequencies, leading to non-physical drops or irregularities in the modal results.

By spreading the contact interaction over multiple surface nodes through RBE3 elements, the load transfer becomes smoother and more physically realistic. This approach prevents the introduction of overly stiff local constraints, stabilizes the eigenvalue problem, and ensures that the computed natural frequencies vary smoothly with the angular position. Consequently, the frequency trends observed in the reduced modal analysis can be confidently attributed to genuine variations in contact stiffness and meshing conditions, rather than to numerical artifacts.

The combined use of distributed contact stiffness and RBE3 kinematic coupling guarantees a robust and stable formulation for both modal and time-domain analyses. It allows the reduced-order model to accurately capture the influence of local contact conditions on global dynamic behavior, while avoiding numerical instabilities that could compromise the interpretation of resonance phenomena and nonlinear effects.

This modeling choice is therefore essential to ensure the reliability of the reduced-order approach and to correctly reproduce the dependence of the system's dynamic characteristics on the gear meshing configuration.

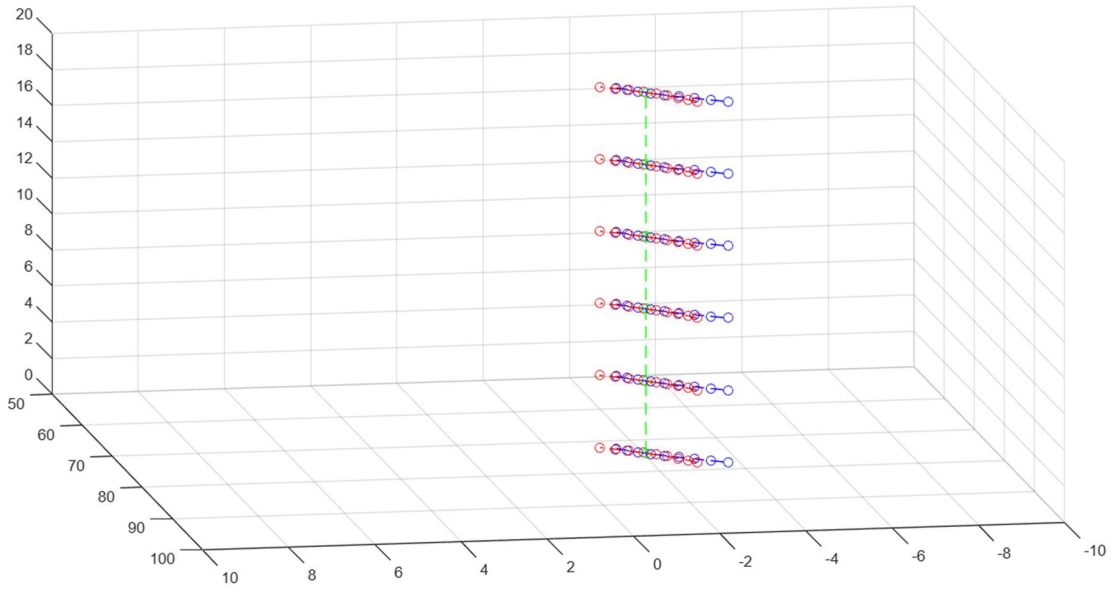


*Figure 15: RBE3 structure during the coupling*

The RBE3 element introduces a structured constraint matrix that relates the degrees of freedom of one master node to those of a set of slave nodes. Unlike rigid constraint formulations, the RBE3 does not impose kinematic equality between nodes, but rather defines a weighted interpolation of the master node motion from the surrounding slave nodes.

Let $\mathbf{u}_s$ be the vector collecting the degrees of displacement of the slave nodes, and $\mathbf{u}_m$ the displacement vector of the master node. The RBE3 kinematic relationship can be written in matrix form as

$$\boldsymbol{u_m = T\, u_s} \tag{22}$$

*Equation 22: RBE3 kinematic relation*

where $\mathbf{T}$ is a transformation matrix whose coefficients are defined by user-specified weighting factors and by the geometric configuration of the slave nodes. Each row of $\mathbf{T}$ corresponds to a master's degree of freedom and is constructed as a linear combination of the corresponding slave degrees of freedom. Importantly, this matrix is generally rectangular and does not introduce additional stiffness or mass terms into the global system matrices.

During the assembly process, the transformation matrix $\mathbf{T}$ is used to project forces applied at the master node onto the slave nodes and, conversely, to reconstruct the master node motion from the slave displacements. As a result, the RBE3 contributes only to the kinematic coupling of the system, without altering its intrinsic dynamic properties.

If contact stiffness were applied directly between isolated nodes or through rigid constraint elements, the resulting stiffness matrix would contain strongly localized terms associated with single degrees of freedom. In reduced-order or rotating contact models, this can lead to the creation of poorly constrained directions or, conversely, to over-constrained local subspaces.

From a numerical standpoint, such configurations generate global stiffness matrices with very small or exactly zero eigenvalues that are not associated with physical rigid-body modes. These so-called *machine zeros* arise due to finite numerical precision and matrix ill-conditioning and manifest themselves as spurious low-frequency modes or sudden drops in the computed natural frequencies.

$$\boldsymbol{F_s = T^T F_m} \tag{23}$$

*Equation 23: force applied on master node and slave node relation*

In the context discussed in the previous sections, these numerical artifacts would appear as irregular frequency dips at specific angular positions, unrelated to any actual physical change in contact conditions. Their occurrence is particularly critical when the model is regenerated cyclically, as even small inconsistencies in constraint enforcement between successive angular steps may introduce discontinuities in the eigenvalue spectrum.

By distributing the contact interaction over multiple slave nodes, the RBE3 avoids the concentration of stiffness and constraint effects on a single degree of freedom. The resulting transformation matrix $\mathbf{T}$has full rank within the constrained subspace and ensures that all master's degrees of freedom are consistently supported by the surrounding structure.

This distributed formulation improves the conditioning of the global stiffness matrix and prevents the emergence of numerically singular directions. Consequently, the eigenvalue problem remains well-posed across all angular configurations, and the computed natural frequencies vary smoothly as a function of the contact position.

In line with the observations presented earlier, the use of RBE3 elements effectively suppresses non-physical frequency drops and eliminates machine-zero-induced anomalies. The remaining variations in the modal results can therefore be confidently attributed to genuine changes in contact stiffness, load sharing, and meshing conditions.

Within the reduced-order framework adopted in this work, the RBE3 formulation plays a crucial role in ensuring both physical realism and numerical robustness. It allows the contact stiffness to be applied in a consistent manner across rotating configurations, supports accurate modal reduction, and guarantees stable time-domain integration.

This confirms that the combination of distributed contact modeling and RBE3 kinematic coupling is essential to overcome the numerical limitations highlighted in the previous analysis and to achieve reliable predictions of the gear system's dynamic behavior.

# ARMONICS EXTRACTION OF COUPLING GEARS

Gear transmissions play a fundamental role in mechanical and automotive systems, where performance, durability, and noise–vibration behavior are critical design and operational aspects. The dynamic interaction between meshing gear teeth generates vibration signals that contain valuable information about the transmission process, manufacturing tolerances, load distribution, and the presence of faults such as wear, pitting, cracks, or misalignment. Consequently, vibration-based signal processing techniques are widely adopted for the analysis, monitoring, and diagnosis of geared systems.

Vibration signals acquired from gearboxes are typically measured in the time domain using accelerometers mounted on the housing. These signals are composed of deterministic periodic components associated with gear meshing and shaft rotation, superimposed on stochastic components arising from structural resonances, background noise, and external excitations. While time-domain analysis provides global indicators such as root mean square or kurtosis values, it does not allow the identification of specific dynamic phenomena related to gear operation. For this reason, frequency-domain and order-based analyses are essential tools in the study of gear vibration behavior.

The classical frequency-domain approach is based on the Fast Fourier Transform, which decomposes a stationary time signal into its spectral components. In gear systems operating at constant speed, the Fourier spectrum exhibits characteristic peaks at the shaft rotational frequency, at the gear mesh frequency, and at their harmonics. The gear mesh frequency is defined as the product of the shaft rotational frequency and the number of gear teeth, and it represents the dominant excitation mechanism in geared transmissions. Additional spectral components may appear in the form of sidebands due to amplitude or frequency modulation caused by transmission errors, load variations, or structural coupling. However, when the rotational speed varies with time, as in run-up or coast-down conditions, the assumption of stationarity is violated, leading to spectral smearing and loss of resolution in the Fourier spectrum.

To overcome these limitations, order analysis provides a more suitable framework for the analysis of vibration signals in rotating machinery. In order analysis, spectral components are expressed in terms of orders, defined as the ratio between a given frequency and a reference rotational frequency. This normalization allows vibration phenomena to be described independently of the absolute rotational speed. As a result, shaft-related excitations appear at integer orders, while gear mesh excitations appear at orders corresponding to the number of teeth. Fractional and multiple orders, known respectively as subharmonics and super harmonics, are often associated with nonlinear effects, localized faults, or intermittent contact phenomena.

The fundamental step in order analysis is the transformation of the vibration signal from the time domain to the angular domain. This process, known as angular resampling, is based on the measurement or estimation of the instantaneous angular position of the rotating shaft, typically

obtained from a tachometer or encoder signal. By resampling the vibration signal at constant angular increments rather than constant time intervals, the resulting signal becomes quasi-stationary with respect to rotational motion. This transformation enables the application of classical spectral analysis techniques in the angular domain, yielding an order spectrum with enhanced resolution and physical interpretability under variable-speed conditions.

Once the signal has been angularly resampled, order tracking techniques can be employed to extract the amplitude and phase evolution of specific orders as functions of time or rotational speed. Order tracking is particularly effective in isolating gear mesh orders and their harmonics, even when multiple rotating components are present. Advanced filtering approaches, such as Vold–Kalman filtering, allow individual orders to be separated with high accuracy while minimizing leakage from neighboring components. This capability is essential for detecting subtle changes in order amplitudes that may indicate the onset of gear damage.

The analysis of harmonics, subharmonics, and super harmonics provides further insight into the dynamic behavior of geared systems. Harmonics of the gear mesh order arise due to nonlinear stiffness variations, contact dynamics, and deviations from ideal involute geometry. Subharmonics, which appear at fractional orders, are often indicative of localized defects such as tooth cracks or spalling, as well as backlash-induced intermittent contact. Super harmonics, corresponding to higher multiples of the fundamental order, may be associated with impact phenomena, strong modulation effects, or the excitation of structural resonances. The identification and interpretation of these components require high spectral resolution and careful signal conditioning.

In practical applications, order analysis is frequently implemented using numerical tools such as MATLAB, which provides dedicated functions for vibration analysis, angular resampling, and order tracking. A typical analysis workflow includes the acquisition of vibration and tachometer signals, the estimation of instantaneous rotational speed, angular resampling of the vibration signal, computation of order spectra, extraction of selected orders, and reconstruction of the corresponding time-domain waveforms. This approach enables systematic and repeatable analysis, making it suitable for both experimental research and industrial condition monitoring.

To further enhance diagnostic sensitivity, order analysis is often combined with complementary signal processing techniques. Time synchronous averaging is used to suppress non-synchronous noise and highlight periodic components related to gear meshing. Envelope analysis is applied to amplitude-modulated signals to reveal fault-induced impulsive behavior. Time–frequency representations allow the identification of transient events and evolving spectral components. The integration of these methods with order-based analysis provides a comprehensive framework for the investigation of gear vibration signals.

The dynamic response of the system, expressed in terms of displacement, velocity, and acceleration, provides a comprehensive description of its behavior across different time scales. Displacement represents the global motion and is typically characterized by smoother and lower-frequency oscillations, reflecting the overall structural deformation. Velocity captures intermediate dynamics, highlighting changes in motion and transitions between different states. Acceleration, on the other hand, is more sensitive to high-frequency content and local effects, making it particularly suitable for identifying rapid variations, impacts, or higher-order dynamic contributions.

Across all three quantities, the system exhibits a consistent evolution from an initial transient phase toward a more stable regime. The initial response is characterized by larger amplitudes and higher variability, which progressively decrease due to damping. While displacement tends to stabilize smoothly, velocity and especially acceleration retain more pronounced oscillatory features, indicating the persistence of dynamic effects even when the overall motion appears stable. This multi-level observation confirms the presence of both global and local dynamic phenomena acting simultaneously within the system.

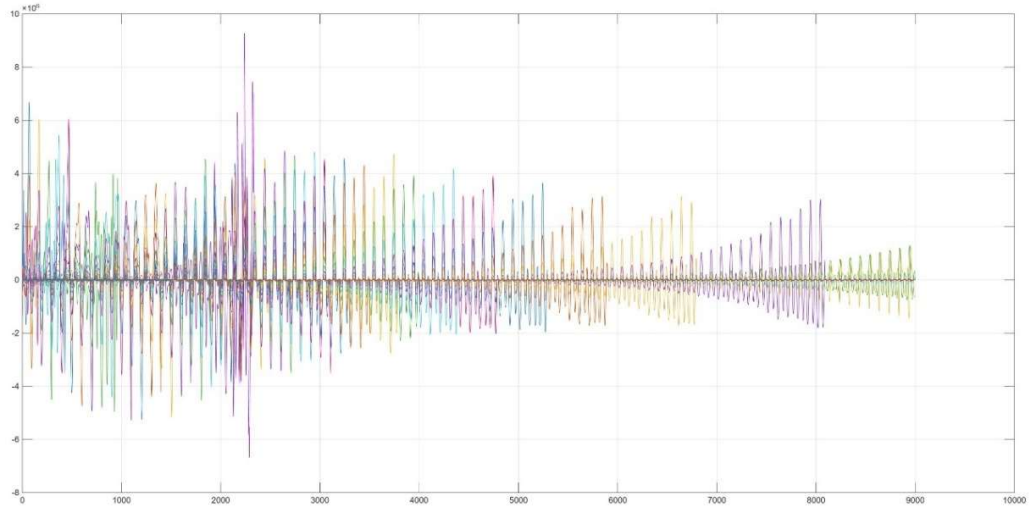

*Figure 16: Accelerations extraction*

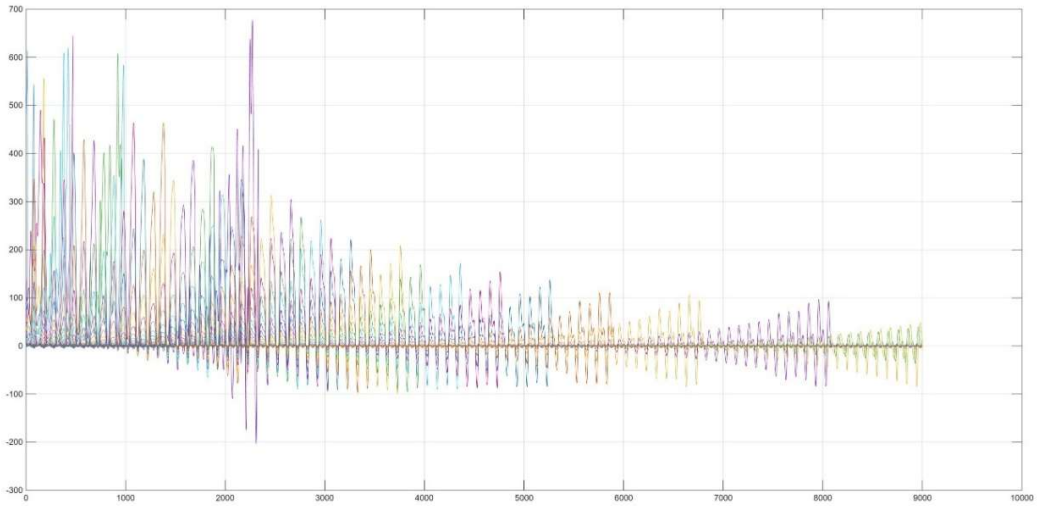

*Figure 17: Speeds extraction*

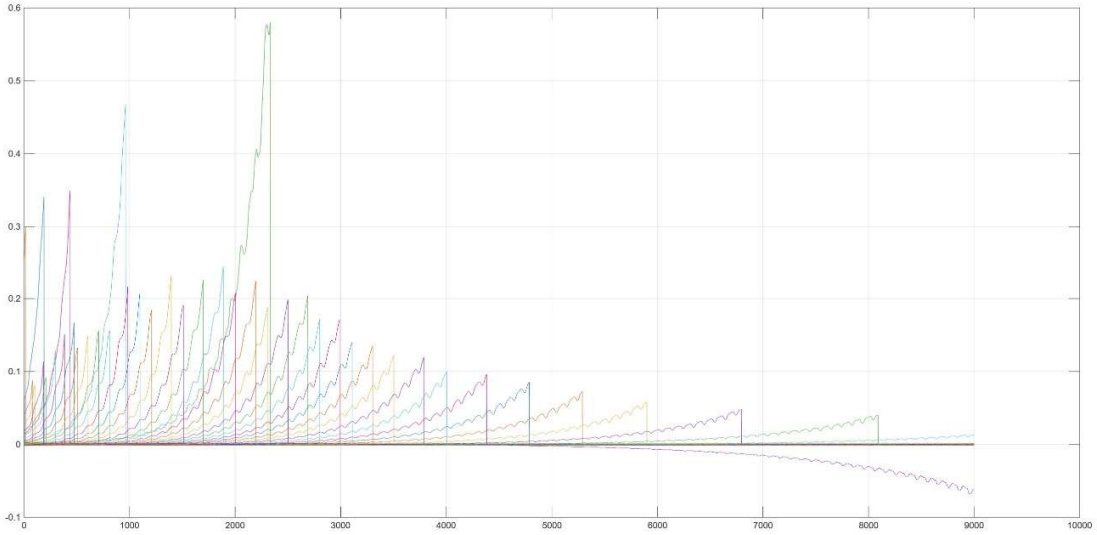

*Figure 18: Displacements extraction*

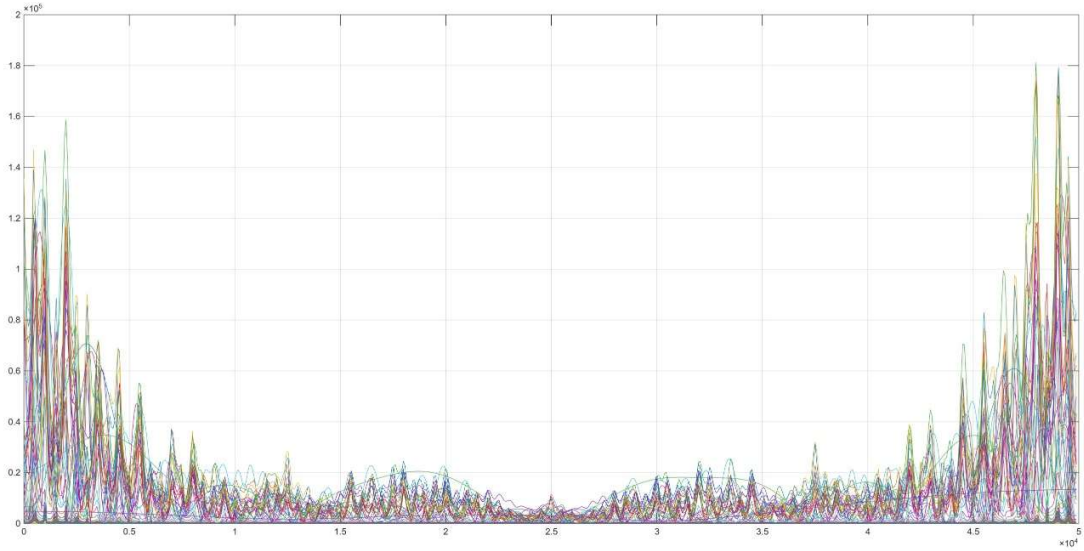

*Figure 19: FFT Gears from 1000 to 5000 rpm at constant speed*

The frequency-domain analysis, performed through the Fast Fourier Transform, provides a complementary perspective by identifying the dominant spectral components of the response. The spectra are generally characterized by distinct peaks at specific frequencies, which correspond to the natural modes of the system. These peaks indicate that the dynamic response is not uniformly distributed across frequencies but is instead concentrated around characteristic values.

At lower frequencies, the spectral content is typically more pronounced, reflecting the dominance of fundamental modes and large-scale motion. As the frequency increases, the amplitude of the spectral components generally decreases, indicating the attenuation of higher-frequency contributions due to inertia and damping effects. However, in some cases, additional peaks or localized increases in spectral amplitude may appear at higher frequencies, suggesting the activation of higher-order modes or localized dynamic phenomena.

Variations in peak amplitude and frequency among different cases reflect changes in system properties and operating conditions. Higher peaks are associated with stronger excitation or reduced damping, while slight shifts in frequency indicate modifications in effective stiffness or mass distribution. The presence of multiple peaks further confirms the multi-degree-of-freedom nature of the system, where several modes can be excited simultaneously.

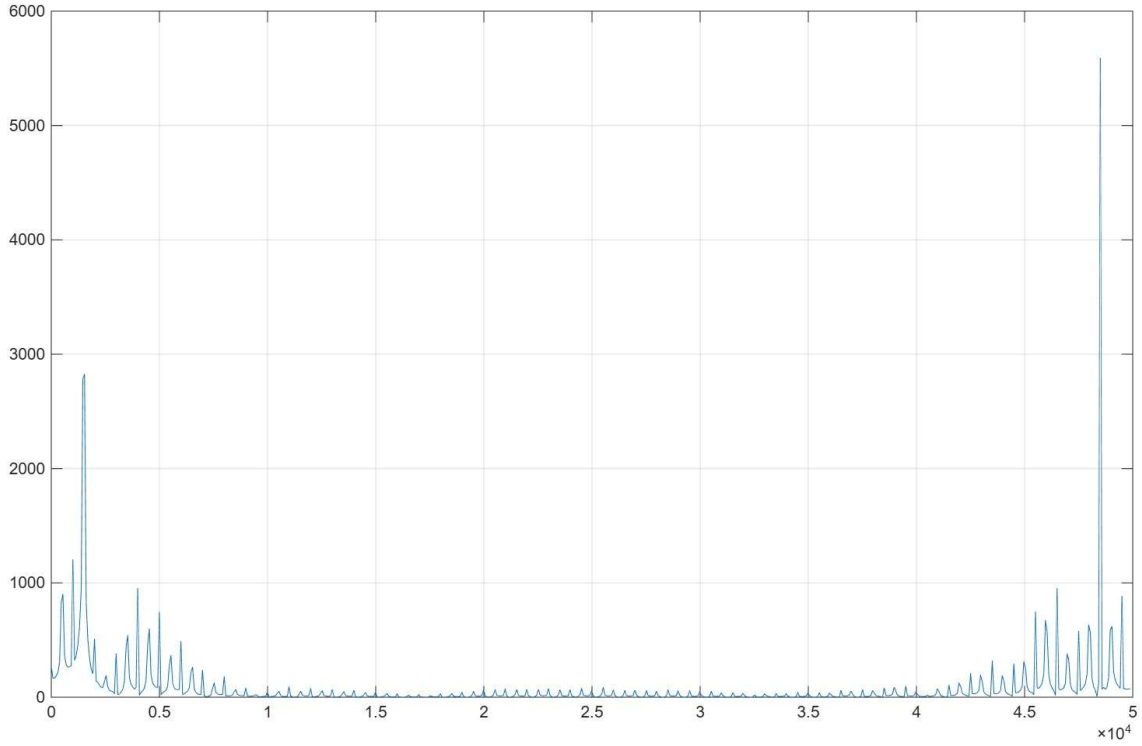


*Figure 20: FFT Gears single case*

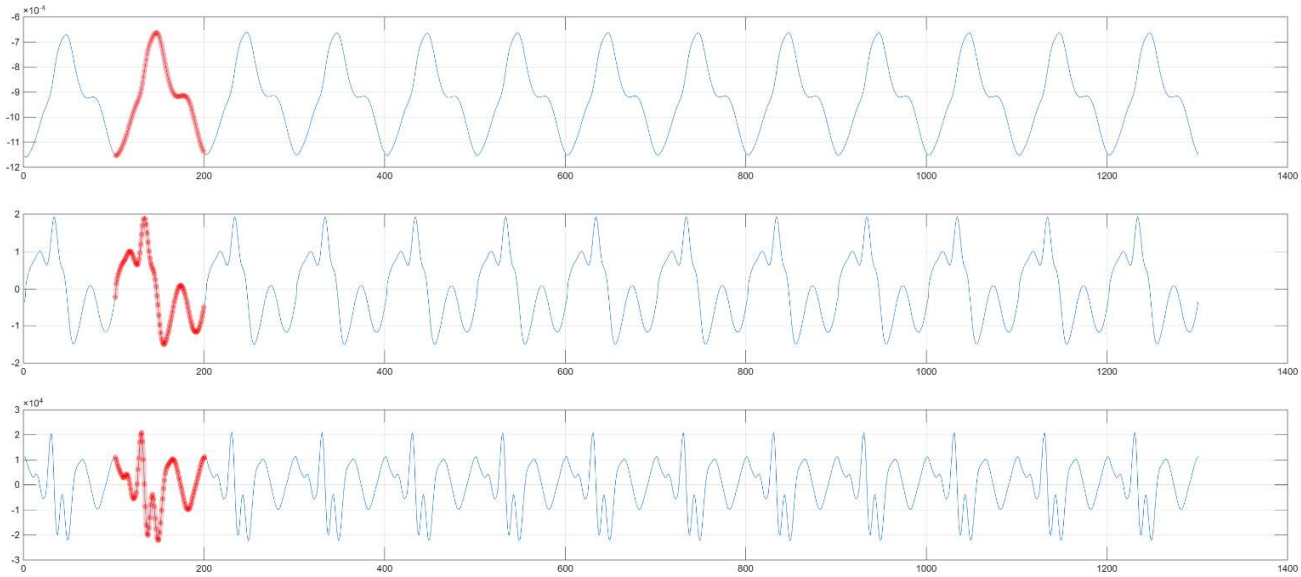

*Figure 21: Kinematic variables analysis*

The acceleration time histories for the selected operating condition exhibit a predominantly periodic response, indicating a stable and repeatable excitation mechanism. The dominant oscillation frequency remains nearly constant over time, suggesting that the system operates close to a steady-state regime governed by its fundamental dynamic modes. Nevertheless, localized deviations from ideal periodicity can be observed. These appear as temporary amplitude modulations and slight distortions of the waveform, revealing the presence of nonlinear effects or interactions between different vibration modes. Such behavior can be associated with transient modal coupling, small variations in contact conditions—such as local stiffness fluctuations or micro-separation—and minor changes in excitation.

A comparison among the three signals highlights distinct dynamic characteristics. One signal exhibit smoother and more sinusoidal oscillations, indicating the predominance of a primary mode. Another shows a more complex waveform, suggesting the presence of additional harmonic components. The third signal presents sharper peaks and greater variability, which may be attributed to stronger contributions from higher-order modes or localized dynamic effects. Despite these differences, the response consistently returns to a stable and repeatable oscillatory pattern, confirming that the observed irregularities are limited in time and do not significantly affect the overall steady-state behavior of the system.

The Dynamic Transmission Error (DTE) represents a key indicator of the vibrational behavior of the system, as it directly reflects the deviation from ideal kinematic transmission between the gears. Its evolution with rotational speed provides valuable insight into the presence of critical operating conditions and resonance phenomena. At lower rotational speeds, it remains relatively small and stable, indicating that the system operates under near-ideal conditions with limited dynamic excitation. In this regime, gear-meshing is regular, and the transmission error is mainly influenced by minor elastic deformations and manufacturing imperfections.

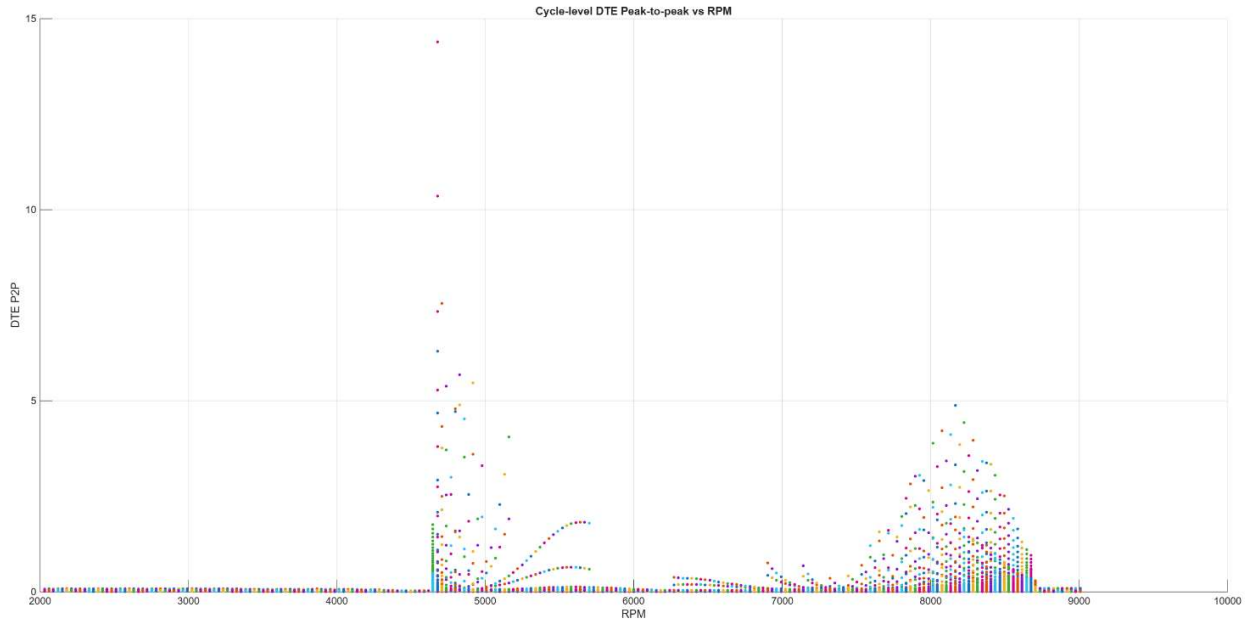


*Figure 22: DTE peaks for FFT different values*

As the rotational speed increases, a marked change in behavior is observed. A pronounced amplification of the DTE occurs within a specific speed range, indicating the onset of a resonance condition. In this region, the excitation frequency associated with gear meshing approaches one of the system's natural frequencies, leading to a significant increase in vibration amplitude. The response also becomes more scattered, suggesting increased sensitivity to initial conditions and the possible presence of nonlinear effects.

Beyond this critical range, the amplitude decreases again, indicating that the system moves away from resonance and returns to a more stable dynamic regime. However, at higher rotational speeds, a secondary region of increased DTE can be identified. This behavior suggests the excitation of additional modes or higher-order dynamic effects, although typically with lower intensity compared to the primary resonance. At very high speeds, the DTE tends to decrease once more, reflecting a reduction in dynamic amplification and a stabilization of the system response.

# CONCLUSIONS

This work has presented the development and validation of a nonlinear reduced-order modeling approach for the dynamic simulation of flexible spur gear systems. The proposed methodology successfully combines high-fidelity finite element modeling with advanced reduction techniques, enabling the accurate representation of gear body flexibility, contact mechanics, and time-varying meshing conditions while drastically reducing computational cost.

The adoption of the Craig–Bampton Component Mode Synthesis method proved effective in preserving the essential dynamic characteristics of the full-order model, reducing the number of degrees of freedom by several orders of magnitude without compromising accuracy. The integration of precomputed time-varying mesh stiffness (TVMS) further enhanced computational efficiency, allowing complex nonlinear dynamic simulations to be performed within practical timeframes.

A key contribution of this work lies in the detailed modeling of contact phenomena, including load-dependent stiffness variation, contact loss, and re-engagement modeled as vibro-impact events. The identification and interpretation of zero-contact-force regions provided important insight into the meshing kinematics and their influence on both static and dynamic responses. The consistent behavior observed across static, modal, and time-domain analyses confirms the physical reliability of the proposed contact formulation.

The introduction of RBE3 elements for distributed contact coupling played a fundamental role in ensuring numerical stability and avoiding artificial stiffness effects or ill-conditioned system matrices. This approach enabled smooth and physically meaningful variations in natural frequencies and prevented the occurrence of non-physical numerical artifacts, such as spurious modes or frequency drops. The model was extensively validated against experimental data, showing excellent agreement in terms of natural frequencies, dynamic transmission error, and nonlinear phenomena such as hysteresis, subharmonics, and superharmonics. The ability of the model to accurately capture resonance behavior and complex dynamic effects demonstrates its robustness and predictive capability.

Finally, the integration of vibration signal analysis techniques, including FFT and order analysis, provided a comprehensive interpretation of the system's dynamic response. The correlation between time-domain behavior, spectral content, and transmission error further confirms the effectiveness of the proposed modeling framework.

Overall, the developed approach represents a powerful and efficient tool for the analysis of geared systems, overcoming the limitations of traditional full-order models. It is particularly well suited for applications requiring repeated simulations, such as design optimization, parametric studies, and condition monitoring.

Future developments may include the extension of the model to helical gears, the incorporation of additional sources of nonlinearity such as friction and lubrication effects, and the integration with real-time diagnostic and control strategies.

# BIBLIOGRAPHY


- Robert G. Parker, "Nonlinear Dynamics of Gear Systems," Annual Review of Fluid Mechanics, vol. 49, pp. 1–25, 2017.
- Faydor L. Litvin and Alfonso Fuentes, Gear Geometry and Applied Theory, 2nd ed., Cambridge University Press, 2004.
- Gérard Genta, Dynamics of Rotating Systems, Springer, 2005.
- J. S. Rao, Rotor Dynamics, 3rd ed., New Age International, 1996.
- Olgierd C. Zienkiewicz, Robert L. Taylor, and J. Z. Zhu, The Finite Element Method: Its Basis and Fundamentals, 7th ed., Elsevier, 2013.
- Klaus-Jürgen Bathe, Finite Element Procedures, Prentice Hall, 1996.
- Roy R. Craig and Michael C. C. Bampton, "Coupling of Substructures for Dynamic Analyses," AIAA Journal, vol. 6, no. 7, pp. 1313–1319, 1968.
- Nathan M. Newmark, "A Method of Computation for Structural Dynamics," Journal of Engineering Mechanics Division, ASCE, 1959.
- K. L. Johnson, Contact Mechanics, Cambridge University Press, 1985.
- William W. Cooley and John W. Tukey, "An Algorithm for the Machine Calculation of Complex Fourier Series," Mathematics of Computation, 1965.
- Randall B. Randall, Vibration-based Condition Monitoring: Industrial, Aerospace and Automotive Applications, Wiley, 2011.
- James I. Taylor, The Vibration Analysis Handbook, Vibration Consultants Press, 1994.
- ISO, ISO 6336: Calculation of Load Capacity of Spur and Helical Gears, ISO Standards, latest edition.
- AGMA, AGMA 2101-D04: Fundamental Rating Factors and Calculation Methods for Involute Spur and Helical Gear Teeth, AGMA, 2004.
- MSC Software, MSC Nastran 2023 – Quick Reference Guide, MSC Software Corporation.
- MathWorks, MATLAB Documentation – Signal Processing Toolbox, The MathWorks Inc., 2025.